A mixed mechano-olfactory code for sniff-invariant odor representations

Authors: Alireza A. Dehaqani*[1,2], Filippo Michelon*[1,2], Luigi Petrucco[1], Paola Patella[2], Eugenio Piasini[3], Giuliano Iurilli[#1]

Affiliations:
[1]Center for Neuroscience and Cognitive Systems, Istituto Italiano di Tecnologia, Rovereto, Italy
[2]CIMeC, University of Trento, Italy
[3]International School for Advanced Studies (SISSA), Trieste, Italy

[*]Equal contribution
[#]Corresponding author

ABSTRACT

A fundamental problem for any sensory system is that the motion of the sensory organ introduces a disturbance in sensory measurement. Nevertheless, animal nervous systems can distinguish and compensate for the sensory consequences of movement by keeping track of them. Hypotheses for estimating the motion of a sensory organ include a corollary discharge associated with motor output and mechanosensory inputs from the moving sense organ. However, how motion-related mechanosensory inputs can reduce motion-dependent sensory ambiguity is unknown. We addressed this question in the olfactory system, where changes in inhalation dynamics alter the sorption of odor molecules by the nasal mucosa and mechanically activate olfactory sensory neurons. We found that changes in inhalation dynamics varied the odor concentration reported by the individual neurons in the piriform cortex. However, the actual odor concentration could be decoded from the population activity regardless of the inhalation dynamics. Dynamics-invariant decoding was possible because piriform cortex neurons have a heterogeneously mixed sensitivity for odor concentration and inhalation dynamics. Thus, the mechanosensory input generated by inhalation expanded the dimensionality of the olfactory encoding space and disentangled the decoding of the actual odor concentration from the disturbance caused by the sniff. Orthogonal integration of motion-related mechanosensory information during the encoding stage may be a canonical strategy adopted by nervous systems to mitigate the sensory ambiguities generated by the motion of the sensory organ.

INTRODUCTION

Animals acquire sensory data while scanning the environment or moving through it. Movement allows animals to assemble a map of the environment and improve the discriminability of stimuli. However, sensory organs' motion represents a potential problem for any sensory system because it distorts the physical properties of the original stimulus[1]. A copy of the movement command sent to the sensory system has been proposed to cancel the sensory effects of the sensory organ's motion[1,2]. In addition, since the sensor's motion can be signaled through mechanosensation, proprioceptive inputs could also have a crucial role, especially when the movement is passive[3]. An important open question is how these motion-related signals combine with sensory inputs to compensate for the sensory consequences of movement without further compromising the representation of the stimulus.

In olfaction, a motion-sensation problem arises with respiration[4,5]. Many species sample airborne chemicals while inhaling air through the nose. Each inhalation offers an instantaneous representation of the olfactory world[6]. An animal tracking an odor plume can thus compare the odor concentration across consecutive inhalations to estimate the distance and direction of an odor source[7–9]. However, the dynamics of an animal's inhalation varies based on the animal's internal state, goal, and external context[6,10,11]. For example, a rapid sniff can determine a two-fold change in the nasal airflow as compared to a slow inhalation[12]. The variability in inhalation dynamics can alter the early representation of an odor in two ways. First, different inhalation dynamics change odorant molecules' retention and migration across the olfactory epithelium[5,13–15]. Second, the pressure generated by the airflow inside the nasal cavities is itself a stimulus that activates a large fraction of olfactory sensory neurons (OSNs) regardless of the presence of an odor[16,17]. Indeed, the magnitude of an OSN response to an odorant scales with the mass flow's velocity inside the nose depending on the strength with which the odorant is sorbed by the nasal mucosa[18,19]. Similarly, mitral/tufted cells (MT) in the olfactory bulb (OB) change their response amplitude to the same concentration of an odor according to the inhalation dynamics[19–26]. Nevertheless, psychophysical experiments in humans and rodents indicate that a subject can learn to report the intensity of an odor regardless of whether the sampling was slow or fast[4,20,21]. How the brain can extract a sniff-invariant representation of an odor is unknown.

Odor information is propagated from the OB to the piriform cortex (PCx), which then broadcasts its output to several downstream brain regions. Upon inhalation, an odor changes the firing rate of PCx neurons according to the neuron's and the odor's identity. Therefore, the population-level representation of an odor occupies an odor-specific region of the PCx encoding space[27,28]. Furthermore, different concentrations of the same odor monotonically change the amplitude and onset of PCx neuron responses. Therefore, a change in odor concentration shifts the population-level representation within the odor-specific region of the encoding space[27,29]. PCx activity is also modulated by the air passage through the nasal cavities, as implied by the observation that each inhalation through the nose entrains the firing rate of PCx neurons[29–35]. However, whether different inhalation dynamics change the PCx representation of an odor is unknown because no study has analyzed PCx odor responses across different types of inhalation. Here we specifically asked whether the inhalation dynamics influences

concentration encoding in PCx and whether and how sniff-invariant olfactory information can be decoded from the population-level activity regardless of the airflow dynamics imposed by each sampling act.

RESULTS

PCx odor responses vary with inhalation dynamics.

To determine the effect of inhalation dynamics on odor intensity encoding in the PCx, we recorded the sniff-by-sniff responses of 660 neurons to five odors presented at two concentrations from the anterior PCx of awake, head-fixed mice (0.01 and 0.1% v./v.; six mice; Fig. 1A-B and Extended Data Fig. 1A). We monitored inhalations through a flow sensor placed in front of the mouse's naris (Fig. 1A); then, we used a semi-unsupervised algorithm to sort inhalations into slow- and fast-type sniffs depending on their dynamics (Fig. 1C-D; Extended Data Fig. 1B-C; see the Methods section).

A total of 36.97% (244/660) of the recorded neurons responded to at least one odor concentration. Inhalation dynamics modulated the latency and amplitude of the odor response in a large fraction of neurons. However, this modulation was not uniform across neurons: 33.24% and 21.93% of neuron-concentration pair responses from odor-responsive neurons increased in amplitude during the first 180 ms of fast and slow inhalation, respectively (Fig. 1E-F). The total fraction of neurons that changed their odor response with inhalation dynamics was significantly higher than that expected by chance (Fig. 1G). We also observed significant sniff-dependent differences in odor responses after restricting the analysis response amplitude within the early 70 ms of inhalation. However, the fraction of sniff-invariant responses increased from 44.83% in the 180-ms window to 59.45% in the 70-ms window (Extended Data Fig. 1D). The non-uniform effect of inhalation dynamics on odor response amplitude was observed in regular spiking (putatively excitatory, RS) and fast-spiking (putatively inhibitory, FS) neurons as well (Extended Data Fig. 1E). Notably, the firing rate change due to variable inhalation dynamics was comparable to that due to a ten-fold concentration increase (Fig. 1H-I). Thus, changes in inhalation dynamics generated a large amount of noise, which could impair the discriminability of odor concentrations on a sniff-by-sniff basis. To test this possibility, we measured a concentration discriminability index (CDI) for each odor-responsive neuron (see Methods section). CDI was computed using odor responses during slow, fast, or both types of inhalation. Mixing responses from slow and fast inhalations decreased CDI, indicating a more significant response variability than the distribution within a single type of inhalation dynamics (Fig. 1J). Thus, the PCx representation of odor intensity changes according to inhalation dynamics. Our next step was to investigate why inhalation dynamics has such a significant impact on PCx odor responses.

PCx neurons encode nasal airflow velocity.

PCx neurons lock their firing rates to the respiratory cycle[29–31,33–35]. Therefore, we hypothesized that inhalation dynamics could change PCx odor responses because each inhalation could provide a non-olfactory input proportional to the nasal airflow. This non-olfactory input could be driven by a sensory

signal originating in the nasal cavity or an efferent motor copy of the inhalation command. Suppose the inhalation input has a sensory origin. In that case, it should be possible to stimulate the nasal cavity with a stream of odorless air independent of the mouse's respiration. To test this hypothesis, we eliminated air passage through the nose via tracheostomy (Fig. 2A). PCx neurons of tracheostomized mice stopped responding to spontaneous inhalation, confirming the nasal origin of inhalation input (Extended Data Fig. 2A). We then mechanically stimulated the nasal epithelium with 150-ms-long airflow pulses delivered a 1 Hz. We tested five different airflow rates within the range of an awake mouse's inhalation[36–39]. Each air pulse triggered a cascade of neural activation in PCx (Extended Data Fig. 2B). Overall, 57.14% of neurons responded to the artificial mechanosensory stimulation of the nasal cavity (144/252 neurons, three mice); furthermore, the neural responses were proportional to airflow velocity (Fig. 2B-C).

This finding prompted us to ask whether PCx neurons also had tuning curves for inhalation dynamics in normally breathing mice (Fig. 2D). To answer this question, we divided the whole range of inhalation dynamics of each mouse into ten bins with an equal number of inhalations; then, we measured the firing rate of a neuron during the inhalations within each bin. This analysis revealed that 78.32% of the PCx neurons encoded the inhalation dynamics with a monotonic change in their firing rate (748/955 neurons, ten mice; Fig. 2E-F). Notably, these mechanosensory tuning curves were heterogeneous across the neural population. Moreover, we found a striking opponent arrangement of the tuning curves; 36.65% of the neurons increased their excitatory responses with the airflow velocity, whereas another 41.67% decreased their responses. This heterogeneous and opponent arrangement of PCx mechanosensory tuning curves indicates that PCx linearly encodes the airflow velocity and may keep the information constant across the full range of nasal airflow experienced by the mouse.

PCx population activity encodes the sniff dynamics.

Population and single neuron raster plots illustrate how each sniff triggers a neural sequence in PCx tiling the respiratory cycle (Fig. 1B and Extended Data Figures 2B and 3A-B). Together with the tuning for the airflow dynamics, these results suggest that PCx may track the periodic dynamics of a sniff. We thus examined whether and how the phase and speed of an inhalation signal are encoded in PCx. To this aim, we turned to a state-space analysis of neuronal population activity. We visualized the dynamics of the population using principal component analysis (PCA). Each inhalation drove the PCx population along a cyclic trajectory that unfolded within a manifold spanned by the first two principal components of the neural activity covariance matrix (Fig. 3A). To determine whether the PCx neural trajectory encoded the inhalation phase, we used a support vector regression (SVR) model to predict the inhalation phase using 10 ms snippets of population spiking activity. The inhalation phase was predicted with high accuracy in all mice (Fig. 3C-D). Notably, information about the inhalation phase depended on inputs from the OB because it could not be decoded using the activity recorded in a non-olfactory area, such as the motor cortex (MCx; Extended Data Fig. 3C-D) and in bulbectomized mice (Extended Data Fig. 3E-F). However, PCx feedback activity was necessary to enforce the neural tiling of the inhalation cycle. AAV-mediated expression of the tetanus toxin light chain (TeLC) in excitatory Emx^+ PCx neurons reduced

cortical postsynaptic transmission without affecting the feedforward input from the OB. After this perturbation, inhalation triggered synchronous and prolonged barrages of activity, consistent with the role of feedback inhibition in taming PCx responses[40]; consequently, the prediction of the inhalation phase from PCx neural activity was worse than in control mice (Extended Data Fig. 3G-H).

Visual inspection of the neural trajectories in control mice also revealed that changing the inhalation dynamics shifted neural activity along a dimension orthogonal to the space encoding the inhalation phase. (Fig. 3B). An SVR model trained on PCx activity during slow inhalations predicted the phase of fast inhalation, indicating that PCx independently encodes the phase and speed of inhalation (Extended Data Fig. 3I); thus, the inhalation phase correlates with the temporal sequence of neural activation in a way that is invariant to the inhalation dynamics.

The above result prompted us to investigate whether the inhalation dynamics could be decoded from the patterns of PCx activity using PCA and decoding analysis (Fig. 3E-F). We found that linear support vector machines (lSVM) could classify an inhalation as fast or slow with high accuracy using a neural pseudo-population pooling the neurons of different mice (Fig. 3F). Similar results were obtained using the neural activity in individual mice (Extended Data Fig. 3J). One possible caveat of this analysis is that differences in neural activity between slow and fast inhalation could be accounted for by different brain states associated with varying breathing rates. To assess whether the linear decoders discriminated between two different inhalation dynamics or two distinct brain states, we repeated the same analysis using the PCx activity of bulbectomized mice that could freely change the dynamics of their inhalations (Fig. 3E). Notably, the linear decoder could still distinguish between slow and fast inhalation after bulbectomy (Fig. 3F). However, the decoding accuracy after bulbectomy was significantly lower than in control mice. Instead, the decoder's accuracy in bulbectomized mice was similar to that of decoders classifying inhalation type using MCx activity in control and bulbectomized mice. Furthermore, the decoding accuracy scaled with the number of neurons used by the decoder in the control mice but plateaued after a few neurons in bulbectomized mice. These observations suggest that the PCx receives brain state-dependent inputs associated with slow and fast sniffing periods. However, these top-down inputs do not carry significant information on inhalation dynamics, provided instead by mechanosensory inputs from the nasal cavity.

Odor and mechanosensory inputs are heterogeneously mixed in PCx.

The above results indicate that PCx mixes odor and mechanosensory responses due to inhalation. Notably, the effect of inhalation dynamics on the firing rate was not uniform across the population of neurons, as indicated by the opponent organization of the tuning curves. This finding suggests the possibility that inhalation signals are randomly distributed to PCx neurons regardless of their odor concentration tuning. Thus, we determined the relationship between the type of inhalation and concentration tuning curves in individual neurons. To this aim, we fitted the PCx odor responses with a generalized linear model (GLM) that included three factors: concentration input, dynamics-dependent mechanosensory input, and the multiplicative interaction between inhalation dynamics and

concentration (Fig. 4A). The multiplicative interaction term was added to capture the variance due the airflow effect on the deposition of odorant onto the nasal mucosa. The GLM analysis revealed that inhalation-dependent mechanosensory inputs had a significant additive effect on odor response (Fig. 4B). Importantly, no uniform relationship existed between how a neuron responded to concentration and inhalation dynamics during the early 180 ms of an inhalation; fast inhalation could increase or decrease a neuron's firing rate regardless of the response to a concentration change. The heterogeneous distribution of mechanosensory sensitivities was similar for RS and FS neurons (Extended Data Fig. 4A-B). By contrast, the interaction between inhalation dynamics and concentration response was small (Fig. 4B and Extended Data Fig. 4A-B), indicating that the mechanosensory input has a more significant effect than airflow-dependent concentration change on PCx response. These results did not change when we restricted the GLM analysis to the early 70 ms of inhalation (Extended Data Fig. 4C). Moreover, similar results were obtained using a non-regularized linear regression model (Extended Data Fig. 4D). Thus, the PCx contains neurons with a heterogenous combination of linear additive selectivity for mechanosensory and olfactory inputs.

Heterogeneous mixed selectivity affords sniff-invariant odor representations.

Heterogenous tuning for odor and mechanosensory inputs has an important implication: the representations of the two modalities do not interfere in the high dimensional space of a large population of neurons (see Methods section for a conceptual proof of this idea in linear encoding systems). To show that this is the case in our data, we turned to PCA and population decoding analysis. PCA decomposition of the population response covariance matrix revealed that the first two principal components (PCs) captured the variance due to the dynamics of inhalation and three odor concentrations (0.01, 0.1, 1% v/v), respectively (Fig. 5A and Extended Data Fig. 5A). To confirm this, we used an lSVM to decode either the inhalation dynamics or the odor intensity from the projections of the PCx responses on the first 15 PCs (Fig. 5B, and Extended Data Fig. 5B-C). Linear decoders could discriminate the inhalation dynamics with high accuracy using the projection of neural activity onto the first PC. In contrast, decoders could not classify an odor's concentration using only the activity explained by the first PC. Moreover, decoders could not classify an odor's identity using only the activity explained by the first PC (Extended Data Fig. 5D), further suggesting that the variance explained by the first PC does not encode olfactory information. Conversely, linear classifiers decoded the odor concentration and identity with high accuracy when they used neural activity along the second and third PCs (Fig. 5B and Extended Data Fig. 5B-D). However, classifiers could not discriminate the inhalation dynamics using the second and subsequent PCs. These results suggest that a population coding of odor concentration may be robust to the correlated noise represented by the fluctuations of population activity due to inhalation.

Importantly, we expected that the concentration-encoding axes shift with the inhalation dynamics but tend to remain parallel because our linear models of the neural responses showed low multiplicative interaction between inhalation dynamics and odor intensity. Thus, we used linear discriminant analysis to find the two axes in the entire population space that maximally separated odor concentrations during

slow and fast inhalations. Notwithstanding the high probability that randomly chosen vectors in high-dimensional space are orthogonal, the angle between the two concentration-encoding axes was closer to zero than the angle between the concentration- and inhalation-encoding axes (Fig. 5C).

These results suggest that the same hyperplane can be fit to discriminate between two concentration representations, regardless of the inhalation dynamics. We thus trained an lSVM to decode an odor concentration using a subset of slow or fast inhalations; then, we tested the performance of the same decoder using held-out inhalations with the same (*cis*-) or other dynamics (*trans*-decoding). A decoder using PCx response projections on the second and third PCs exhibited similar *cis*- and *trans*-decoding performances, suggesting that PCx has sniff-invariant representations of odor intensity (Fig. 5D and Extended Data Fig. 5D). Next, we tested the linear decoders on the untransformed PCx responses, thus removing the possibility that the decoder could leverage the denoised representations provided by PCA; this *trans*-decoder could still predict the odor concentration, generalizing across inhalation dynamics (Fig. 5D and Extended Data Fig. 5E). Similar results were obtained using the first 70 ms and 180 ms of each inhalation (Extended Data Fig. 5F).

To determine whether a subset of neurons with sniff-invariant concentration encoding was the only driver of good generalization performance across inhalation dynamics, we compared the performances of concentration *trans*-decoders using neurons with different levels of mechanosensory input. To this aim, we sorted PCx neurons based on their mechanosensory sensitivity; the latter was assessed by fitting the sniff-by-sniff odor responses with a linear regression model with a concentration and a mechanosensory regressor. Neurons with a mechanosensory regressor coefficient within 0 ± 0.75 standard deviations were included in the sniff-invariant population, whereas an equal number of remaining neurons were included in the mechano-sensitive population (Fig. 5E). A comparison of the classification accuracies of *trans*-decoders using sniff-invariant and mechano-sensitive populations revealed that sniff-invariant concentration information was present even in a population without sniff-invariant neurons (Fig. 5F). However, sniff-invariant neurons may provide more sniff-invariant information than mechano-sensitive neurons only during the early part of an inhalation; the previous analysis would overlook this difference because it was based on the spike counts within the first 180 ms of each inhalation. Thus, we asked how well concentration decoders using sniff-invariant or only mechano-sensitive neurons could generalize across inhalation dynamics during the time course of an inhalation. To this aim, we partitioned the population neural activity in twenty consecutive time bins (10 ms/bin), tiling the first 200 ms of an inhalation; then, we ran *cis*- and *trans*-decoders using sniff-invariant or mechanosensory-sensitive neurons for each time bin. This analysis showed that a population including only mechanosensory-sensitive neurons already encodes sniff-invariant concentration information during the initial part of an inhalation (Fig. 5G).

Because odor concentration can also be decoded from the temporal sequence of PCx neural responses, we investigated whether linear decoders could generalize across inhalation dynamics using the timing of odor responses from the onset of odor inhalation[27]. Furthermore, given that our data showed that PCx

contains information on the inhalation phase, we also tested linear decoders using the action potential phase relative to a sniff. Notably, the latter code does not use extrinsic time information as the sniff phase information is intrinsic in the state of the population activity, as shown above (Fig. 3A). Both the time- and phase-based decoders could predict odor intensity during same-dynamics inhalations with accuracies similar to those of rate-based decoders (Extended Data Fig. 5G).

The heterogeneity of mechanosensory and olfactory tuning determined the degree of decoding generalization across inhalation dynamics. To show this, we performed PCA and decoding analysis on neural sub-populations with correlated sensitivity to mechanosensory and olfactory inputs. PCA embeddings of the odor responses showed that representations of odor concentrations become ambiguous across inhalation dynamics in these sub-populations (Fig. 5H). Thus, a *trans*-decoder performed at chance level if it could only use the activity of a neural population with correlated sensitivity for mechanosensory and olfactory inputs (Fig. 5I). Instead, using a population with uncorrelated selectivity disentangled the population representations of inhalation dynamics and odor concentration, thus allowing a *trans*-decoder to generalize odor intensity discrimination across inhalation dynamics (Fig. 5H-I). These results indicate that the heterogenous distribution of mechanosensory inputs to PCx neurons orthogonalizes the effect of those inputs on population odor representations.

Integrating the inhalation signal marginalizes the motion-dependent olfactory reafference.

Changes in airflow velocity alter the odorant concentration profile in the nasal cavity; consequently, the odor representation shifts along the odor-encoding axis. However, the increase in dimensionality due to the mechanosensory input orthogonally offsets the concentration representation shift on parallel odor encoding axes (Fig. 5L). Thus, a decoder may learn a tilted decision boundary and classify the real odor intensity regardless of the odorant perturbation generated by the airflow. We probed this feature afforded by the mechanosensory input by simulating the responses of a population of neurons with varying levels of inhalation-dependent concentration change and mechanosensory input. To generate the surrogate distribution of responses, we used the odor and inhalation covariate weights obtained by fitting our recorded neural responses with a linear regression model. We simulated different levels of interaction between airflow and odorant retention by assuming that the inhalation-driven change in concentration (ΔIC) is proportional to the initial concentration and the inhalation dynamics (see Methods section). We varied ΔIC over a two-fold range to approximate the measured nasal airflow rate range[12]. PCA embedding showed that odor representations were ambiguous in this simulated population when there was no inhalation input (Fig. 5J); for example, an increase in odor concentration could not be distinguished from an increase in inhalation dynamics. Therefore, decoders trained on the responses during slow and fast inhalations classified the odor intensity worse than decoders trained using only one inhalation dynamics as the simulated disturbance of the airflow on the concentration increased (Fig. 5K). However, supplementing this population with neurons with randomly assigned mechanosensory responses was sufficient to reduce ambiguity and recover the actual concentration for any ΔIC (Fig. 5 J-K).

Together, these results indicate that providing PCx neurons with independent information about the airflow dynamics inside the nasal cavity offsets the sensory variance generated by different inhalations. Consequently, a downstream area can learn the same distributed code and read the odor concentration from a population of PCx neurons regardless of how the animal samples the odor.

DISCUSSION

Changes in inhalation dynamics alter the retention of odors in the nasal cavities[5,13–15] and generate a mechanosensory stimulation of the olfactory epithelium[16,17]. However, the perception of odor intensity can be sniff-invariant[4,20,21]. Our study shows that the PCx generates a sniff-invariant representation of odor concentration that can be learned and read at the population level. This is because PCx activity embeds a mechanosensory signal from the nasal cavity proportional to the dynamics of inhalation. At the population level, the encoding of this mechanosensory input is independent of the odor encoding; hence the PCx effectively augments the dimensionality of its coding space. This geometry orthogonalizes the mechanosensory disturbance determined by different airflows and may distinguish an actual concentration increase from a change in odor adsorption caused by different inhalation dynamics.

Prior work showed that the faster inhalation of an odor reduces the onset of OB mitral cell responses and changes their amplitude similarly to an increase in odor concentration[20,21]. Here, we found that fast inhalation dynamics either enhances or reduces the response amplitude of more than 50% of PCx neurons. A brain area downstream of the olfactory system may nevertheless read-out the environmental concentration of an odor by relying only on those PCx neurons that do not vary their response with the inhalation dynamics. Indeed, we found sniff-invariant neurons in PCx; how these neurons generate sniff-invariant odor representations remains to be determined because prior studies did not find sniff-dynamics-invariant mitral and tufted neurons in the OB[20,21]. One possibility is that some PCx neurons may read out the OB input using a relative timing code. Since the airflow generated by inhalation also activates neurons that are not tuned for the inhaled odor, it was hypothesized that the relative timing between the responses of odor-responsive and odor-unresponsive mitral cells could distinguish an actual increase in concentration from a faster sniff[21]; this coding strategy is consistent with the known sensitivity of PCx neurons to the relative timing of their OB inputs[41]. Our findings demonstrate, however, another possible and complementary algorithm that solves the sniff-invariance problem using the information encoded by the entire population of PCx neurons; this solution uses a rate code and leverages the geometry afforded by the independent combination of odor and inhalation inputs. With this encoding strategy, the inhalation-driven activity does not degrade the odor information, analogously to what happens in the case of noise correlations that are orthogonal to the signal of interest. In addition, the airflow-dependent perturbations of the odor concentration are displaced on the parallel olfactory-encoding axes generated by different inhalation dynamics, allowing the learning of sniff-invariant discrimination boundaries.

The geometrical solution to the motion-sensation problem uncovered here may not necessarily be specific to the olfactory system. Indeed, orthogonal dimensions for encoding movements have been

found in other sensory cortices, like the primary visual cortex (V1)[42]. The orthogonal encoding of orofacial movements and visual stimuli most likely derives from the heterogenous combination of visual and non-visual inputs. For example, V1 neurons independently encode the direction of a drifting grating and a saccade[43]. Similarly, we analyzed an Allen Brain Observatory dataset and found that V1 neurons independently encode the pupil size and the contrast of a visual stimulus (Extended Data Fig. 6). Furthermore, we found that similar to the organization of olfactory and mechanosensory tuning curves in PCx, the heterogenous mixing of visual and non-visual inputs in V1 disentangled the representations of pupil size and visual contrast. Some active behaviors are associated with pupil dilation[44,45]; however, a large pupil size determines a loss of image contrast and visual acuity due to aberrations[46,47] and higher luminance affecting retina processing[48]. Whether the independent response to pupil size may be helpful to keep the signal-to-noise in V1 invariant should be tested. Our results indicate an essential role for motion-related mechanosensory signals in mitigating the disturbances due to varying inhalation rates. We expect mechanosensory and proprioceptive signals to play a similar role in other sensory cortices, especially for passive movements. For example, psychophysical experiments in humans suggest that inflowing proprioceptive signals might reduce the perceived extent of the visual smear generated by passive head and eye movements[49]. Interestingly, the visual cortex receives information about head movements through additive vestibular inputs[50]. Building on our results, we propose that embedding independent, motion-informative mechanosensory inputs into sensory distributed codes could be a canonical strategy to offset the consequences of sensory organ movements on sensation.

Author contribution:
Conceptualization: G.I.; *Methodology:* F.M., A.A.D and G.I; *Software:* A.A.D, L.P. and G.I.; *Formal analysis:* A.A.D, L.P., P.P, E.P. and G.I.; *Investigation:* F.M., P.P. and G.I.; *Resources:* G.I.; *Data curation:* A.A.D. and P.P.; *Writing:* G.I.; *Visualization:* P.P. and G.I.; *Supervision:* G.I.; *Project administration:* G.I.; *Funding acquisition:* G.I.

Acknowledgements
G.I. is supported by the Giovanni Armenise-Harvard C.D.A.; L.P. is supported by an EMBO Postdoctoral Fellowship.

Data and code availability
All data and code will be made available upon reasonable request.

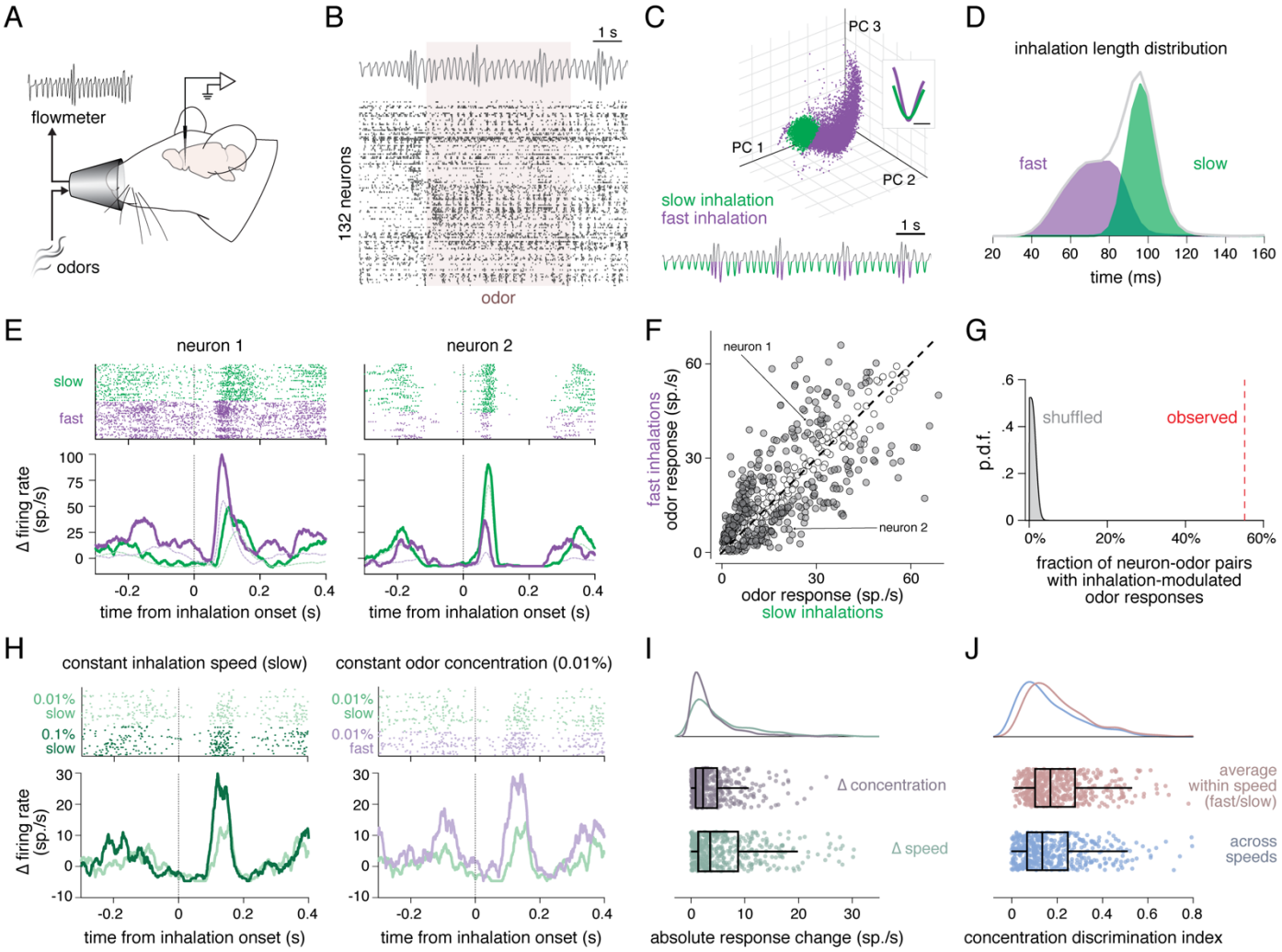

Figure 1. PCx odor responses vary with inhalation dynamics.

a. Experimental setup for PCx recordings paired with odor delivering and sniff monitoring.

b. Example of simultaneous PCx activity and sniffing behavior. External flow sensor signal (top) and spiking raster plot of 132 neurons from one recording (bottom). The shaded area indicates where the odor was delivered.

c. Sorting slow and fast inhalations. PCA plot of inhalation waveforms sorted via gaussian-mixture model-hierarchical clustering (top). Each data point corresponds to an inhalation. Example sniffing signal in **b** with sorted inhalations (bottom). Green and purple indicate slow and fast clusters, respectively (total number of inhalations: 25056; number of slow inhalations: 15163; number of fast inhalations: 9893).

d. Distribution of slow and fast inhalation lengths. The gray curve corresponds to the length distribution before inhalation sorting.

e. Examples of odor concentration responses during slow and fast inhalations. Raster plot (top) and peri-inhalation time histogram (PITH, 10 ms gaussian kernel; bottom) are shown for two neurons. Dashed lines indicate PITH in the absence of odor. Rasters and PITHs are aligned to the inhalation onset (vertical dotted line).

f. Scatterplot of the odor concentration responses (average firing rate in 180 ms window and across slow or fast inhalations; five odors, 0.01 and 0.1% v./v. concentration; n = 725 responses) for all odor-responsive neurons (p-value < 0.01; n = 244 neurons, six mice). Each data point corresponds to a neuron-concentration pair. The two concentration responses in **e** are indicated. Filled, significant response difference between fast and slow inhalation; empty, no statistical difference (rank-sum test, two-tails, p-value < 0.01).

g. Fraction of neurons changing odor concentration response with inhalation dynamics (red vertical line) and null distribution obtained by shuffling 1000 times the inhalation dynamics label for each odor response.

h. Examples of responses to different odor concentrations and different inhalation dynamics. Left, responses to 0.01 % (light green) and 0.1 % (dark green) v./v. averaged across all inhalations. Right, responses to slow (light green) and fast (light purple) inhalations of 0.01% v./v. odor. Raster plots and PITHs for an example neuron are shown. Rasters and PITHs are aligned to the inhalation onset (vertical dotted line).

i. Absolute change in firing rate due to a slow-to-fast switch in inhalation of 0.01 % odor and a 0.01-to-0.1% change in odor concentration. Each data point corresponds to a neuron-odor pair (n = 500 neuron-odor pairs; only odor-responsive neurons).

j. Concentration discrimination index (CDI) calculated using odor concentration responses within and across inhalation dynamics (P < 10-4, rank-sum test). Within-inhalation-dynamics CDIs are averages of the only-slow and only-fast CDIs. Across-inhalation dynamics CDIs were calculated using all odor concentration responses of a neuron regardless of the inhalation dynamics. Each data point corresponds to a neuron-odor pair (n = 500 neuron-odor pairs; only odor-responsive neurons).

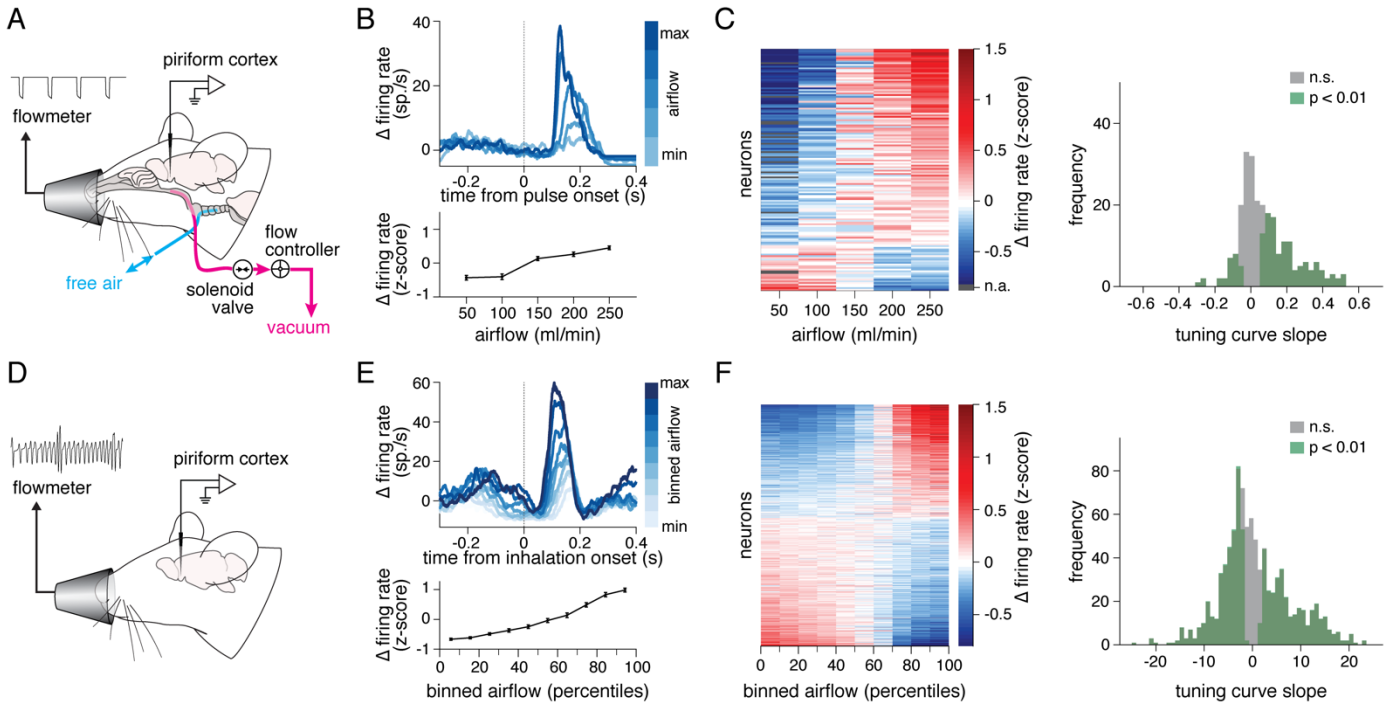

Figure 2. PCx neurons encode nasal airflow velocity.

a. Experimental setup for artificial airflow stimulation of the nasal cavity in anesthetized mice.

b. Example neuron responding to five different airflow velocities. Peri-event time histograms for each airflow velocity (top) and tuning curve (bottom) are shown.

c. Left, raster map of the airflow velocity tuning curves of all PCx neurons (n = 144 tuned neurons). Right, distribution of the slopes of the airflow tuning curves. The shaded area indicates the distribution region containing slopes significantly different from zero (tuned neurons). Positive slope: 117 of 252 neurons; negative slope: 27 of 252 neurons ($p<0.01$, ANOVA).

d. Experimental setup for PCx recordings paired with monitoring of spontaneous breathing in awake mice.

e. Left, example neuron responding to ten different airflow dynamics. Peri-inhalation time histograms for each inhalation dynamics (top) and tuning curve (bottom) are shown.

f. Left, raster map of the airflow dynamics tuning curves of all PCx neurons. Right, distribution of the tuning curve slopes. The shaded area indicates the distribution region containing slopes significantly different from zero. Positive slope: 350 of 955 neurons; negative slope, 398 of 955 neurons ($p<0.01$, ANOVA).

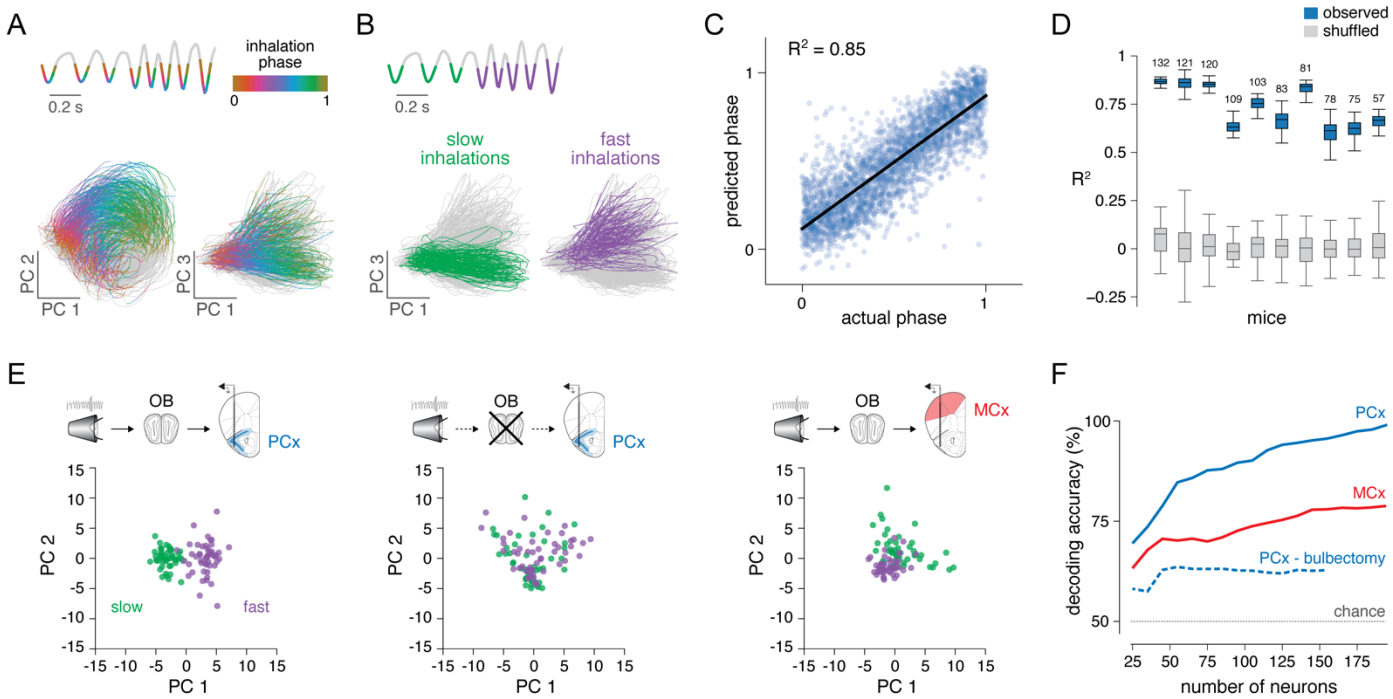

Figure 3. PCx population activity encodes the sniff dynamics.

a. PCA embedding of the neural population trajectories during individual respiratory cycles for an example mouse (time bin length: 10 ms). The inhalation phase is color-coded according to the scheme in the inset plot on the top (inhalation onset: 0, inhalation offset, 1; example respiration trace is shown). The exhalation portion of the respiratory cycle is colored gray.

b. Same neural trajectories as in **a** color-coded according to the inhalation dynamics. Green: slow; purple, fast.

c. Scatterplot of the actual and predicted inhalation phase for an example mouse (n = 120 neurons). The inhalation phase was predicted with a cross-validated support vector regression model using the inhalation-driven neural trajectories in the space spanned by a number of principal components sufficient to explain more than 50% of the variance. The goodness of the prediction was evaluated by calculating the squared correlation coefficient between the actual and predicted phase (R^2).

d. Goodness of inhalation phase prediction (R^2) using the PCx neural trajectories of all mice (blue). Null distributions (gray) were obtained by shuffling the order of the neural activity time bins within each inhalation. Medians, 25th-75th percentiles (box), and 5th-95th percentiles (whiskers) are shown. The number of neurons used for phase prediction is indicated for each mouse.

e. PCA embedding of the pseudo-population responses to single inhalations in the PCx of control (left) and bulbectomized (center) mice and in the MCx cortex of control mice. The pseudo-population was obtained by pooling 155 neurons from four (bulbectomized PCx) or ten (control PCx and MCx) mice.

Control PCx and MCx neurons were simultaneously recorded from the same mice. Each data point represents a single population vector response. A random sample of responses is shown.

f. Decoding accuracy of SVM classifier predicting the inhalation dynamics as a function of the neurons included in the analysis; classifiers used PCx (red) or MCx (blue) activity in the control condition (solid line) and after bulbectomy (dotted line).

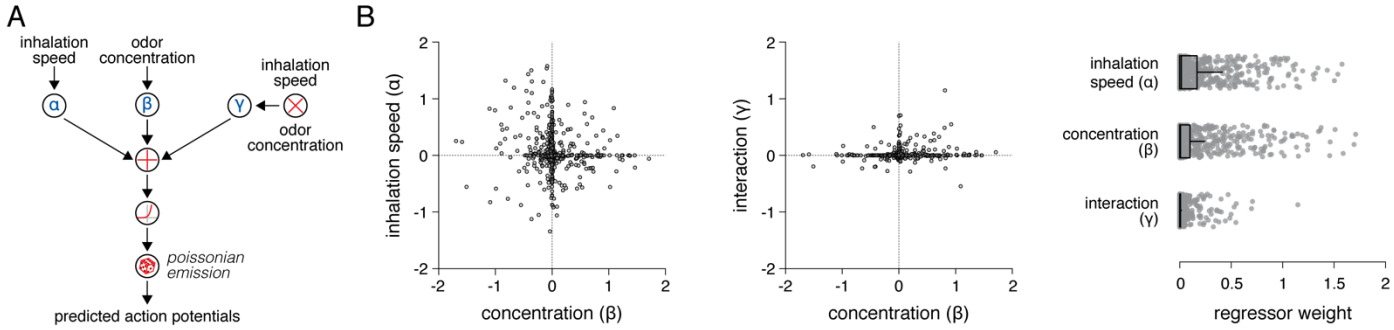

Figure 4. Odor and mechanosensory inputs are heterogeneously mixed in PCx.

a. Left, schematic of the generalized linear model (GLM) used to predict the odor response based on inhalation dynamics (slow: 0, fast: 1), odor concentration (0.01, 0.1, 1% v.v.), and their interaction. The GLM was regularized with an elastic-net method (goodness-of-fit $R^2 = 0.94$).

b. Left, scatterplot of the concentration and inhalation factor regression coefficients. Center, scatterplot of the regression coefficients for the concentration and interaction factor. Each data point represents a neuron-odor pair (n = 928 neuron-odor pairs; 2 odors; 464 neurons; 4 mice). Right, distribution of the absolute value of the regression coefficients for inhalation dynamics, odor concentration, and their interaction (n = 928 neuron-odor pairs; 2 odors; 464 neurons; 4 mice).

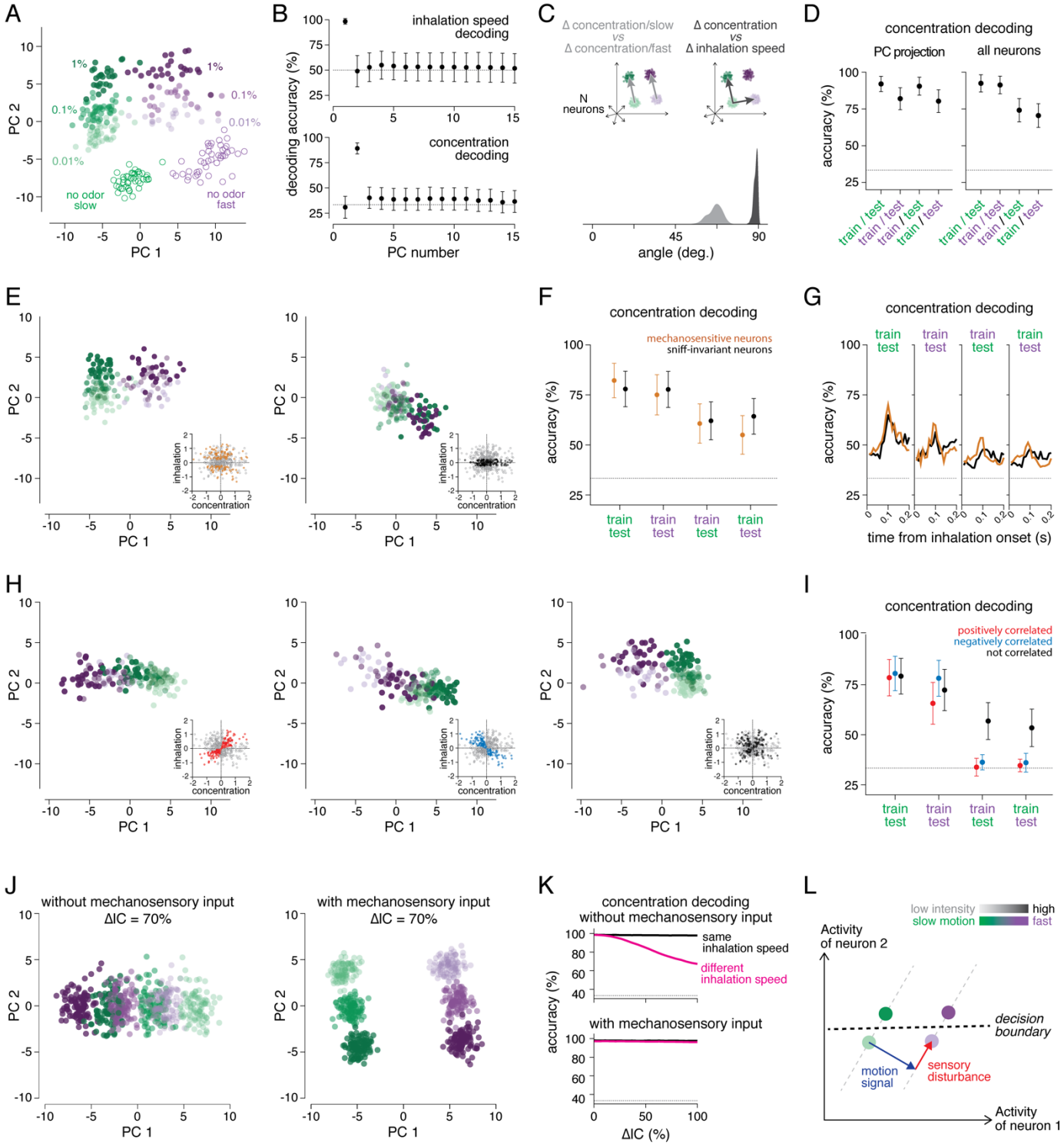
A
1%
1%
0.1%
0.1%
0.01%
0.01%
no odor slow
no odor fast
PC 2
PC 1
B
inhalation speed decoding
concentration decoding
decoding accuracy (%)
PC number
C
Δ concentration/slow vs Δ concentration/fast
Δ concentration vs Δ inhalation speed
N neurons
angle (deg.)
D
concentration decoding
PC projection
all neurons
accuracy (%)
train / test
E
inhalation
concentration
F
concentration decoding
mechanosensitive neurons
sniff-invariant neurons
accuracy (%)
train
test
G
concentration decoding
accuracy (%)
time from inhalation onset (s)
H
I
concentration decoding
positively correlated
negatively correlated
not correlated
accuracy (%)
J
without mechanosensory input
ΔIC = 70%
with mechanosensory input
ΔIC = 70%
K
concentration decoding
without mechanosensory input
same inhalation speed
different inhalation speed
with mechanosensory input
accuracy (%)
ΔIC (%)
L
low intensity
high
slow motion
fast
Activity of neuron 2
decision boundary
motion signal
sensory disturbance
Activity of neuron 1

Figure 5. PCx population odor representations are sniff-invariant.

a. PCA embeddings of pseudo-population responses to three different concentrations of an example odor (eucalyptol; 0.01, 0.1, and 1% v.v.) during slow (green) and fast (purple) inhalations. The pseudo-population was obtained by pooling 464 neurons from four mice. Each dot represents the pseudo-population response in a 180 ms window starting at the inhalation onset. A random sample of responses is shown.

b. Decoding accuracy of inhalation speed (top) and odor concentration (bottom) using the projection of the pseudo-population odor responses on each of the first fifteen PCs (n = 464 neurons; three concentrations; two inhalation speeds). Mean ± standard deviation is shown. See Extended Data Fig. 5C for a scree plot of the variance explained by the first 15 PCs.

c. Angle between vector pairs representing concentration changes (light grey) and vector pairs representing a concentration change and an inhalation dynamics change (dark grey).

d. Left, concentration decoding accuracy within (*cis*-decoder) and across (*trans*-decoder) inhalation speed using the pseudo-population response projections onto the second and third PCs (n = 464 neurons; three concentrations). Right, concentration decoding accuracy within and across inhalation speeds using pseudo-population responses without PCA. *Cis*-decoders were trained on slow (green) or fast (purple) inhalations and tested on held-out slow or fast inhalations, respectively. *Trans*-decoders were trained on slow (green) or fast (purple) inhalations and tested on held-out fast or slow inhalations, respectively. Mean ± standard deviation is shown.

e. PCA embeddings of concentration responses using a neural pseudo-population with and without sniff-invariant neurons. Mechanosensory sensitivity was estimated as the regression coefficients of a two-factor (inhalation and concentration) linear model fitted to single-neuron responses. Insets: scatterplots of the inhalation and concentration regression coefficients for all recorded neurons (n = 464 neurons). Each data point corresponds to a neuron. The subset of neurons in the population response vector is highlighted by color: black, the sub-population of neurons with sniff-invariant neurons; orange, the sub-population of neurons without sniff-invariant neurons. To build the pseudo-population single-inhalation response vector, an equal number of neurons was randomly sampled from each sub-population (n = 143 neurons). A random sample of responses is shown.

f. Concentration decoding accuracy within (*cis*-decoder) and across (*trans*-decoder) inhalation speed using a pseudo-population with (black) and without (orange) sniff-invariant neurons. To build the pseudo-population single-inhalation response vector, an equal number of neurons was randomly sampled from each sub-population (n = 143 neurons). Mean ± standard deviation is shown.

g. Concentration decoding accuracy within and across inhalation speed over the time course of an inhalation. *Cis*- and *trans*-decoders like those used in panel **f** were used to discriminate odor concentration within and across inhalation dynamics using the population activity in 10 ms bins tiling the first 200 ms of an inhalation. The mean accuracy obtained using a sniff-invariant (black) and mechanosensory-sensitive population (orange) is shown.

h. Population concentration representations for different relationships between inhalation and concentration sensitivities. The PCA embedding of concentration responses is shown for three pseudo-populations with positive (left), negative (center), and no correlation (right) between the inhalation and concentration sensitivity. Insets: scatterplots of the inhalation and concentration regression coefficients for all recorded neurons (n = 464 neurons). Each data point corresponds to a neuron. The subset of neurons included in the population response vector is highlighted by color: red, sub-population of neurons with positive correlation; blue, sub-population of neurons with positive correlation; black, sub-population of neurons without correlation. To build the pseudo-population single-inhalation response vector, an equal number of neurons was randomly sampled from each sub-population (n = 143 neurons). A random sample of responses is shown.

i. Concentration decoding accuracy within (*cis*-decoder) and across (*trans*-decoder) inhalation speed using three pseudo-populations with different relationships between concentration and inhalation sensitivities. The color indicates the relationship between concentration and inhalation sensitivities across the pseudo-population as in **e**: red, positive correlation; blue, negative correlation; black, no correlation. To build the pseudo-population single-inhalation response vector, an equal number of neurons was randomly sampled from each sub-population (n = 143 neurons). Mean ± standard deviation is shown.

j. Inferred effect of the inhalation input on the concentration representation in the presence of inhalation-driven alteration of the odorant concentration. Left: PCA embedding of population concentration responses with a 70% inhalation-driven concentration change (ΔIC) and without inhalation input. Center: PCA embedding of population concentration responses with a 70% ΔIC and inhalation input. Population responses were simulated using the inhalation and concentration regression coefficients estimated from the actual data to generate new single-neuron responses. The ΔIC was artificially added to the concentration covariate of the model as a term proportional to the actual concentration and the inhalation speed.

k. Concentration decoding accuracy for increasing levels of inhalation-dependent ΔIC without (top, purple) and with (bottom, purple) inhalation input across different inhalation speeds. Decoding accuracies within similar inhalation dynamics (black) are shown to highlight the importance of the inhalation signal for sniff-invariant concentration representation.

l. Integration of a motion-related signal within a sensory area increases the dimensionality of the encoding space, offsets the motion-dependent sensory disturbance, and thus affords motion-invariant stimulus decoding.

Extended data

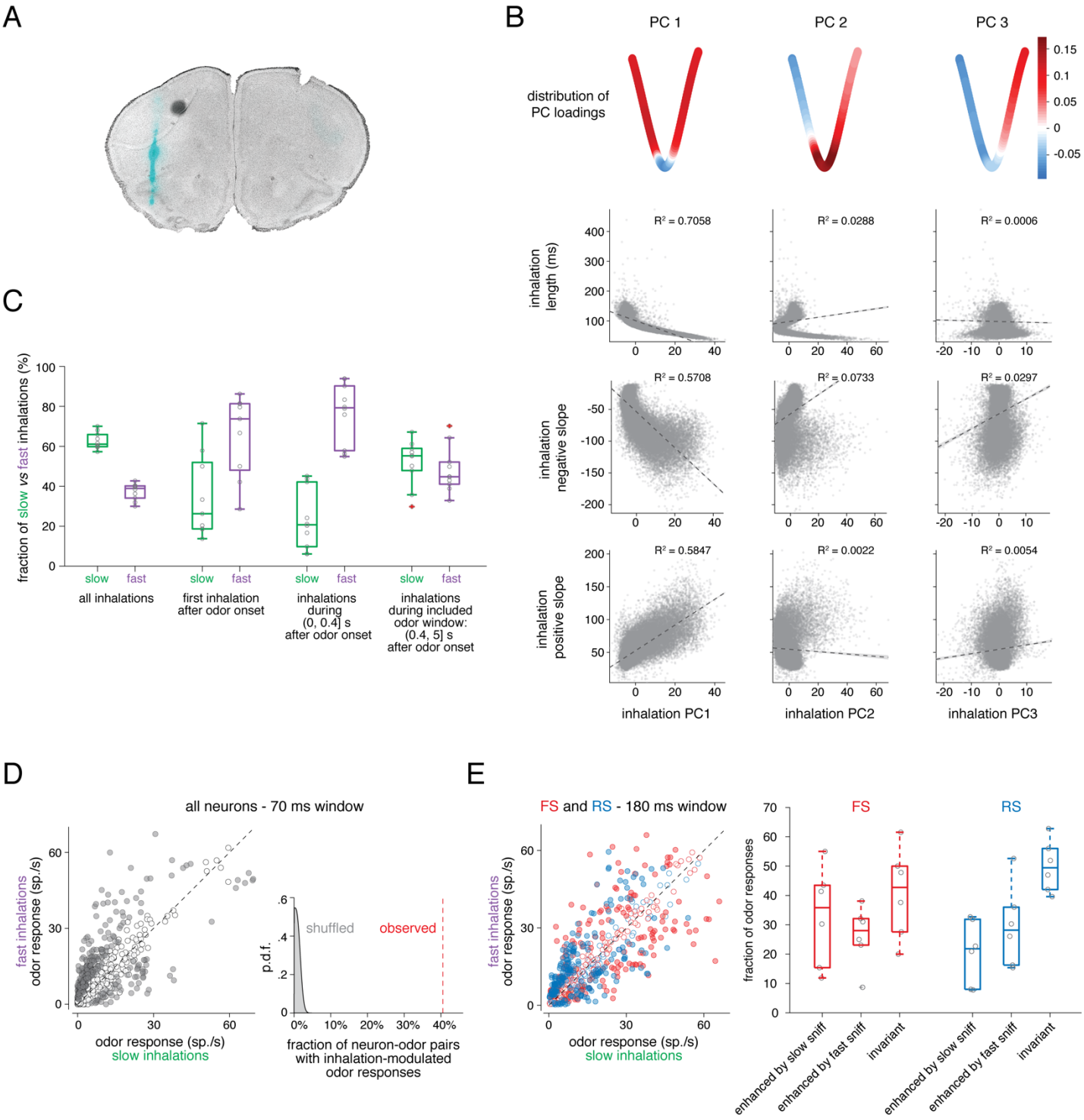

Extended Data Figure 1

a. Example of coronal section indicating the placement of Neuropixels in anterior PCx (cyan).

b. Top row: loadings of the first three PCs of normalized inhalation waveforms; bottom rows: correlation between first (left), second (middle), and third (right) PCs and inhalation length (first row), descending slope waveform (second row) and ascending slope (third row) of the inhalation waveform. Each data point corresponds to an inhalation. The first PC was sufficient to capture most of the inhalation dynamics.

c. Boxplots showing the fraction of slow and fast inhalation types observed during the whole experiment, the first inhalation of an odor, the early 400 ms of the odor window, and the odor window analyzed for the main results. Each data point represents a single experiment's mean fraction (N = 10 mice). Boxplots indicate the median, 25th and 75th percentile.

d. Left: scatterplot of the odor concentration responses like in Fig. 1F but for the early 70 ms window of inhalation (mean firing rate across slow or fast inhalations; five odors, 0.01 and 0.1% v./v. concentration; n = 725 responses) for all odor-responsive neurons (p-value < 0.01; n = 244 neurons, six mice). Each data point corresponds to a neuron-concentration pair. Filled, significant response difference between fast and slow inhalation; empty, no statistical difference (rank-sum test, two-tails, p-value < 0.01). Right: fraction of neurons changing odor concentration response with inhalation dynamics (red vertical line) in the early 70 ms window and null distribution obtained by shuffling 1000 times the inhalation dynamics label for each odor response.

e. Left: scatterplot of the odor concentration responses (n = 725 neuron-concentration pairs) like in Fig. 1F but after sorting neurons in RS (blue, n = 434 neuron-concentration pairs) and FS (red, n = 291 neuron-concentration pairs). Right: boxplots showing the fraction of odor concentration responses significantly enhanced by a fast or a slow inhalation or are sniff-invariant (p-value < 0.01, rank-sum test) for RS and FS neurons. Each data point represents the fraction in a single experiment (N = 6 mice). Boxplots indicate the median, 25th and 75th percentile.

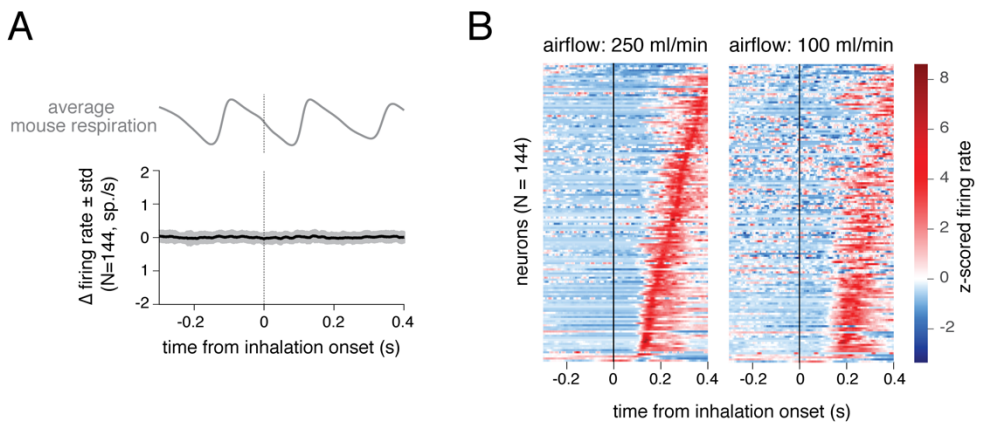

Extended Data Figure 2

a. Grand-average peri-inhalation time histogram (PITH) aligned to the self-generated inhalation onset in tracheostomized mice (n = 144 neurons responsive to nasal airflow stimulation, three mice). Self-generated inhalations were detected using a piezo sensor embedded in a chest belt.

b. Rastermaps of peri-event time histograms (PETH) in tracheostomized mice. PETHs were aligned to the onset of a 150 ms-long airflow pulse applied to the back of the rhino-pharynx. Each row corresponds to the PETH of an individual neuron (n = 144 neurons, three mice). Left, PETH upon stimulation with a 100 ml/min airflow pulse; right, PETH upon stimulation with a 250 ml/min airflow pulse. PETHs were sorted bottom-up based on the latency to the peak of the response to the 250 ml/min airflow pulse.

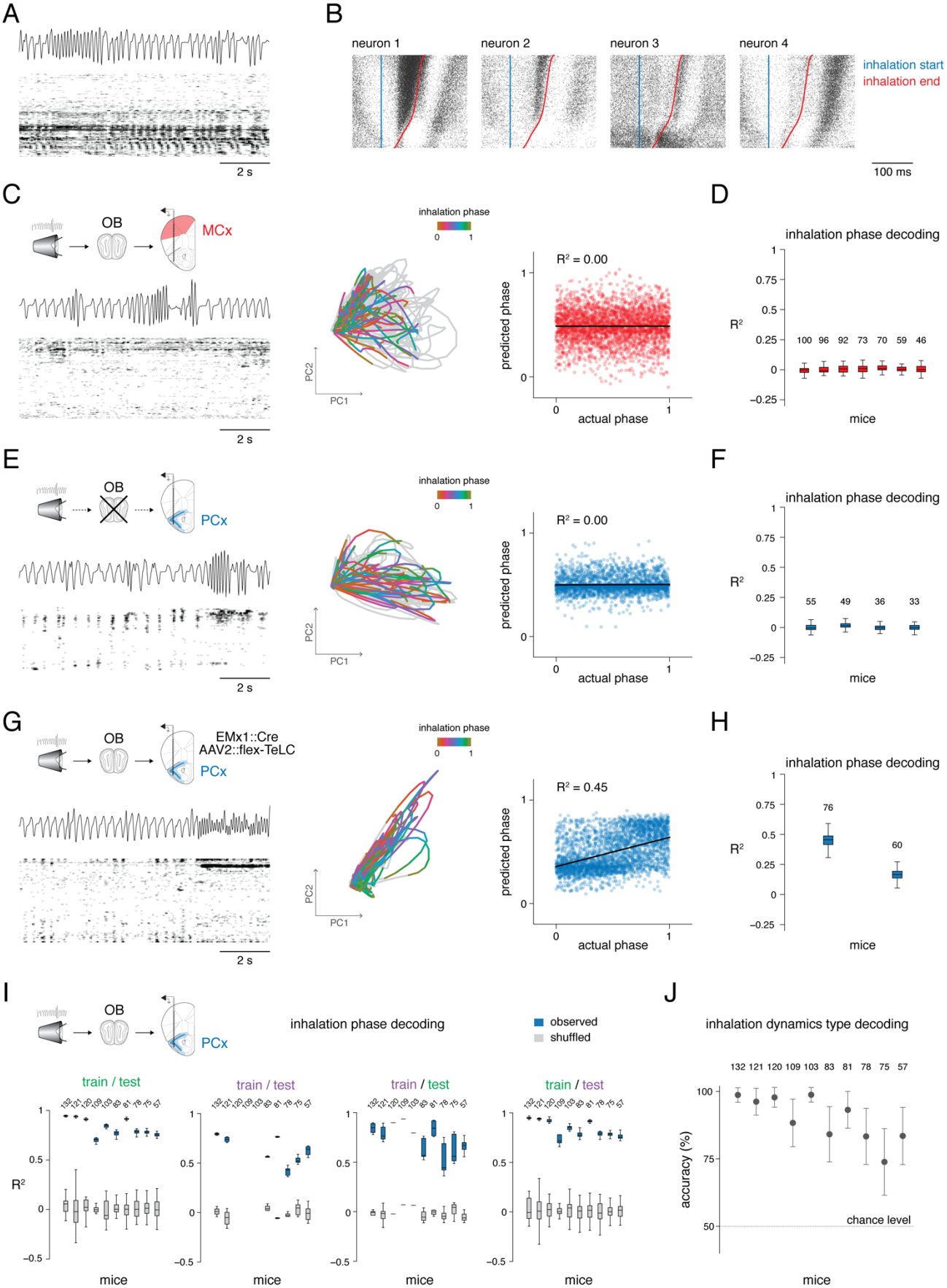
A
2 s
B
neuron 1
neuron 2
neuron 3
neuron 4
inhalation start
inhalation end
100 ms
C
OB
MCx
2 s
inhalation phase
0
1
PC2
PC1
R² = 0.00
predicted phase
actual phase
D
inhalation phase decoding
R²
100 96 92 73 70 59 46
mice
E
OB
PCx
2 s
inhalation phase
PC2
PC1
R² = 0.00
predicted phase
actual phase
F
inhalation phase decoding
R²
55 49 36 33
mice
G
OB
EMx1::Cre
AAV2::flex-TeLC
PCx
2 s
inhalation phase
PC2
PC1
R² = 0.45
predicted phase
actual phase
H
inhalation phase decoding
R²
76
60
mice
I
OB
PCx
inhalation phase decoding
observed
shuffled
train / test
train / test
train / test
train / test
132 121 120 109 103 83 81 78 75 57
R²
mice
mice
mice
mice
J
inhalation dynamics type decoding
132 121 120 109 103 83 81 78 75 57
accuracy (%)
chance level
mice

Extended Data Figure 3

a. Example of simultaneous PCx activity (n = 121 neurons) and sniffing behavior. External flow sensor signal (top) and spiking raster plot of X neurons (bottom). Each inhalation triggers a cascade of neural activity.

b. Example rasters of four PCx neurons from the recording in a. Each row represents the spiking activity during an inhalation. The blue dots indicate the inhalation onset, whereas the red dots indicate the end of the inhalation. Inhalations were sorted top-down according to the length of the respiratory cycle. Note the sequential activation of the four neurons upon inhalation. Furthermore, increasing the inhalation speed decreases the inhalation response of the first two neurons, increases the inhalation response of the third neuron, and has a negligible impact on the fourth neuron.

c. Left: Example of simultaneous MCx activity (n = 100 neurons) and sniffing behavior. Center: PCA embedding of the neural trajectory over multiple respiratory cycles; color indicates the inhalation phase, and gray corresponds to the exhalation phase of the respiratory cycle. Right: scatterplot of the actual and predicted inhalation phase for an example mouse using the activity of MCx neurons. The inhalation phase was predicted with a cross-validated support vector regression model (SVR) using the inhalation-driven neural trajectories in the space spanned by a number of principal components sufficient to explain more than 50% of the variance. The goodness of the prediction was evaluated by calculating the squared correlation coefficient between the actual and predicted phase (R^2).

d. Evaluation of inhalation phase prediction (R^2) using the MCx neural trajectories of all mice. Medians, 25th-75th percentiles (box), and 5th-95th percentiles (whiskers) are shown. The number of neurons used for phase prediction is indicated for each mouse.

e. Left: Example of simultaneous PCx activity (n = 49 neurons) and sniffing behavior in a bulbectomized mouse. Center: PCA embedding of the neural trajectory over multiple respiratory cycles.
Right: scatterplot of the actual and predicted inhalation phase. Note the barrages of synchronous neural activity and the absence of coherence between respiratory cycles and PCx activity.

f. Evaluation of inhalation phase prediction (R^2) using the neural trajectories of all bulbectomized mice. The number of neurons used for phase prediction is indicated for each mouse.

g. Left: Example of simultaneous PCx activity (n = 76 neurons) and sniffing behavior after silencing PCx synaptic transmission by expressing TeLC in Emx1+ neurons. Center: PCA embedding of the neural trajectory over multiple respiratory cycles. Right: scatterplot of the actual and predicted inhalation phase.

h. Evaluation of inhalation phase prediction (R^2) using the neural trajectories of Emx1-TeLC mice. The number of neurons used for phase prediction is indicated for each mouse.

i. Inhalation phase decoding within and across inhalation dynamics types. Cross-validated SVRs were trained on random selections of slow (green) or fast inhalations (purple) and tested on held-out inhalations of the same type (*cis*-decoders) or the other type (*trans*-decoders). The quality of the prediction for individual mice is reported as the linear regression coefficient between the actual and the

predicted phase. The number of neurons used for each mouse is indicated. The similarity in performance between *cis*- and *trans*-decoders indicates that the phase information encoded by the temporal sequence of neural activation is robust to neuron-specific changes in firing rate due to changing inhalation speed.

j. Inhalation speed decoding in individual mice. Cross-validated linear support vector machine models using the population pattern activity in the first 180 ms of an inhalation classified the current inhalation as slow- or high-speed type with high accuracy. Mice are sorted as in panel **i**. The number of neurons used for each mouse is indicated.

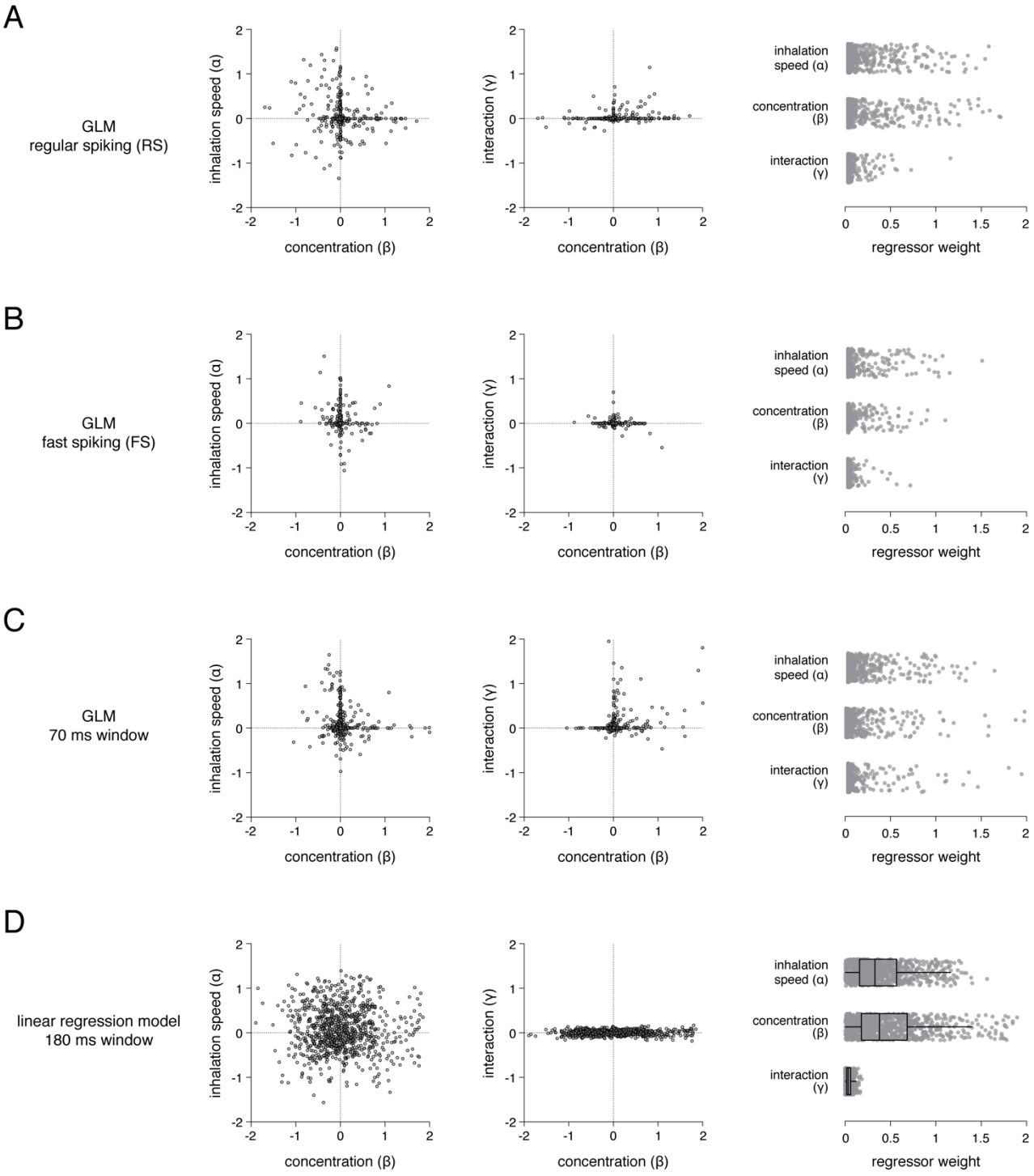

Extended Data Figure 4

a. Left, scatterplot of the regularized GLM regression coefficients for the concentration and inhalation factor in RS neurons using the 0-180 ms window of inhalation. Center, scatterplot of the regression

coefficients for the concentration and interaction factor. Right, distribution of the absolute value of the regression coefficients for inhalation dynamics, odor concentration, and their interaction. Each data point represents a neuron-odor pair (n = 928 neuron-odor pairs; 2 odors; 464 neurons; 4 mice).

b. Same as **a** but for FS neurons.

c. Left, scatterplot of the regularized GLM regression coefficients for the concentration and inhalation factor in all neurons using the 0-70 ms window of inhalation. Center, scatterplot of the regression coefficients for the concentration and interaction factor. Right, distribution of the absolute value of the regression coefficients for inhalation dynamics, odor concentration, and their interaction. Each data point represents a neuron-odor pair (n = 928 neuron-odor pairs; 2 odors; 464 neurons; 4 mice).

d. Left, scatterplot of the linear regression coefficients for the concentration and inhalation factor in all neurons using the 0-180 ms window of inhalation. Center, scatterplot of the regression coefficients for the concentration and interaction factor. Right, distribution of the absolute value of the regression coefficients for inhalation dynamics, odor concentration, and their interaction. Each data point represents a neuron-odor pair (n = 928 neuron-odor pairs; 2 odors; 464 neurons; 4 mice). The regression coefficients for two odors (odor 1: eucalyptol and odor 2: pinene) are shown. Goodness-of-fit, R^2: 0.78.

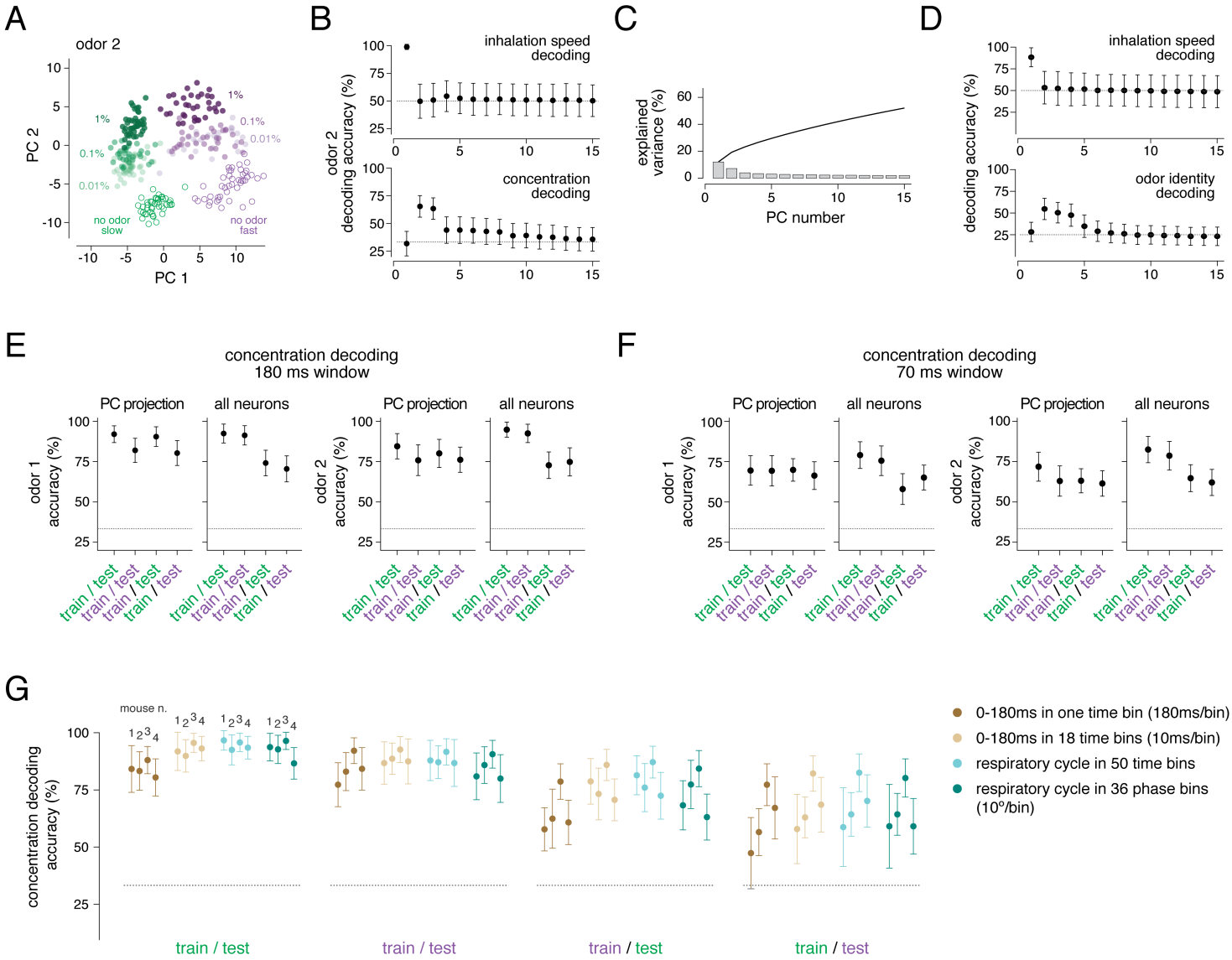

Extended Data Figure 5

a. PCA embeddings of pseudo-population responses to three different concentrations of another example odor (pinene; 0.01, 0.1, and 1% v.v.) during slow (green) and fast (purple) inhalations. The pseudo-population was obtained by pooling 464 neurons from four mice. Each dot represents the pseudo-population response in a 180 ms window starting at the inhalation onset. A random sample of responses is shown.

b. Decoding accuracy of inhalation speed (top) and odor concentration (bottom) using the projection of the pseudo-population odor responses on each of the first fifteen PCs (n = 464 neurons; three concentrations; two inhalation speeds). Mean ± standard deviation is shown.

c. Scree plot of the variance explained by the first 15 PCs of the covariance matrix, including the responses of 464 neurons to the two odors (eucalyptol and pinene) presented at three concentrations. These are the PCs used in Fig. 5B and Extended Data Fig. 5B.

d. Decoding accuracy of inhalation speed (top) and odor identity (bottom) using the projection of the pseudo-population odor responses on each of the first fifteen PCs (four odors; two inhalation speeds). Mean ± standard deviation is shown. The data used for this analysis are from a different set of experiments where four odors were presented to mice without changes in concentration.

e. Concentration decoding accuracy for two odors (odor 1: eucalyptol and odor 2: pinene) using the PCx activity during the 0-180 ms window of inhalation. The decoding accuracy using the PC projections and all neurons are shown for each odor. Left, concentration decoding accuracy within (*cis*-decoder) and across (*trans*-decoder) inhalation speed using the pseudo-population response projections onto the second and third PCs (n = 464 neurons; three concentrations). Right, concentration decoding accuracy within and across inhalation speed using pseudo-population responses without PCA. *Cis*-decoders were trained on slow (green) or fast (purple) inhalations and tested on held-out slow or fast inhalations, respectively. *Trans*-decoders were trained on slow (green) or fast (purple) inhalations and tested on held-out fast or slow inhalations, respectively. Mean ± standard deviation is shown.

f. Same as in **e** but using the 0-70 ms window of inhalation.

g. Comparison of the accuracy of a linear decoder across four different coding schemes. Dark brown: average population activity in the 0-180 ms window of a respiratory cycle; 0 ms: inhalation onset. Light brown: neural population trajectory during the 0-180 ms window; the neural activity during the 180 ms window was binned in 18 bins of equal duration (10 ms), and a population vector was built using the average activity of each neuron during a given time bin; finally, the 18 vectors were concatenated to obtain the population trajectory. Light teal: neural population trajectory during the entire respiratory cycle; the respiratory cycle was binned in 50 time bins of equal duration within the cycle; the time bin duration varied across respiratory cycles due to the different duration of each cycle; the 50 population vectors were concatenated to obtain the population vector during a respiratory cycle. Dark teal: neural population trajectory during the entire respiratory cycle using the phase instead of the timing; the respiratory cycle was binned in 36 phase bins of equal length (10º); the 36 population vectors were concatenated to obtain the population trajectory during a respiratory cycle. Mean ± standard deviation is shown for four mice.

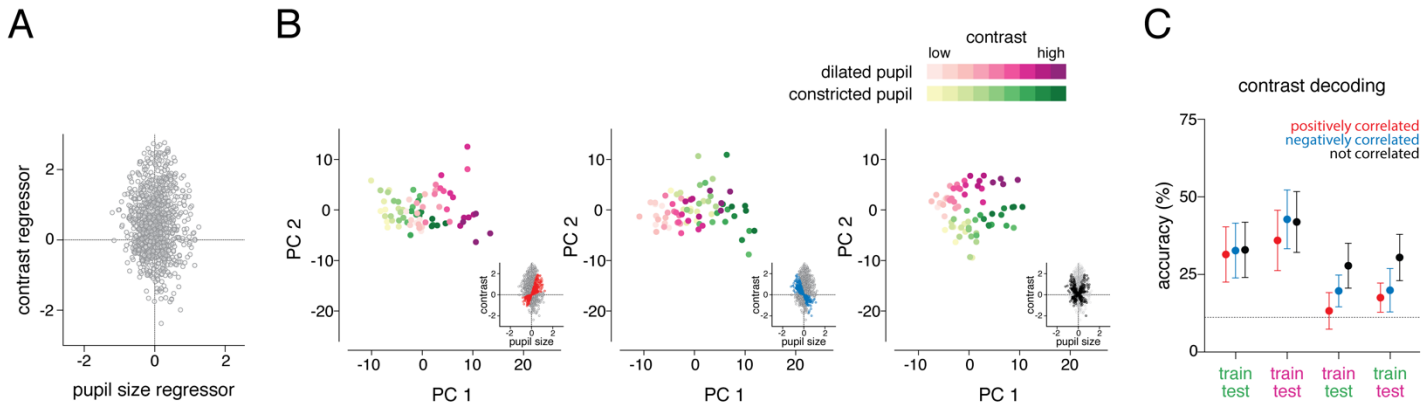

Extended Data Figure 6

a. Heterogenous distribution of sensitivities for visual contrast and pupil size in V1. A scatterplot of the linear regression coefficients for contrast and pupil size is shown. Each data point represents a neuron (n = 1085 neurons from 18 sessions). The model was fitted to the visual responses to a drifting grating (orientation: 0°; spatial frequency: 0.04 cycle/°; temporal frequency: 2 Hz) presented at nine logarithmically scaled contrast levels between 1 and 100% of the monitor contrast range. These data were downloaded from the Allen Brain Observatory database (Stimulus set: Functional connectivity).

b. PCA embedding of the visual responses to drifting gratings (orientation: 0°; spatial frequency: 0.04 cycle/°; temporal frequency: 2 Hz) with nine different contrasts and upon two pupil sizes is shown for V1 pseudo-populations with positive (left), negative (right) and uncorrelated sensitivities to visual contrast and pupil size. Insets: scatterplots of the contrast and pupil size regression coefficients for all neurons (n = 1085 neurons). Each data point corresponds to a neuron. The subset of neurons included in the population response vector is highlighted by color: red, sub-population of neurons with positive correlation; blue, sub-population of neurons with positive correlation; black, sub-population of neurons without correlation. An equal number of neurons was randomly sampled from each sub-population (n = 293 neurons) to build the pseudo-population response vector. A random sample of responses is shown.

c. Heterogenous sensitivity to pupil size and visual inputs provides V1 with pupil-size invariant contrast encoding. Contrast decoding accuracy within (*cis*-decoder) and across (*trans*-decoder) pupil sizes using three pseudo-populations with different relationships between contrast and pupil size sensitivities. The type of relationship between contrast and pupil size sensitivities across the pseudo-population is indicated by the color as in b: red, positive correlation; blue, negative correlation; black, no correlation. An equal number of neurons was randomly sampled from each sub-population (n = 293 neurons) to build the pseudo-population response vector. An equal number of trials (n = 4) was used for the 18 contrast and pupil size combinations. Mean ± standard deviation is shown.

METHODS

Ethical compliance

All experimental manipulations were performed according to Italian legislation (DL 26/214, EU 63/2010, Ministero Della Sanità, Roma) and FELASA recommendations for the care and use of laboratory animals. Animal research protocols were reviewed and consented to by the animal care committee of the University of Trento and Italian Ministry of Health (authorization no. 159/2020-PR).

Animals

We used 6-9 weeks old C57BL/6J and Emx1:Cre mice of both sexes (Jackson Laboratory). Mice were co-housed with their littermates (2-4/cage) and maintained on a 12 hr/12 hr light/dark cycle with food and water ad libitum. Four C57BL/6 mice were used for the two odors/three concentrations (0.01, 0.1, and 1% v./v.) experiments; two C57BL/6 mice were used for the four odors/two concentrations (0.01 and 0.1% v./v.) experiment; four C57BL/6 mice were used for the odor identity experiments; three C57BL/6 mice were used for the artificial inhalation experiment; four C57BL/6 mice were used for the bulbectomy experiment; two Emx1:Cre mice were used for the TeLC experiment.

Surgical procedures

Animals were anesthetized with isoflurane (3% induction, 1.5% maintenance) and placed on a custom-made feedback-controlled heating pad. Pre-operative analgesia was induced through intramuscular injection of a bolus (4μl/g) of carprofen (0.05%)/dexamethasone (0.01%) and scalp infiltration of a tetracaine solution (0.05%). Post-operative analgesia was provided through carprofen diluted in the water bottle (Rimadyl, 134µl/100ml) for 48 hours following the procedure. Silicone-based eye ointment was applied on the eyes to protect the corneas during the surgery.
Anesthetized mice were mounted in a stereotaxic frame. The scalp was shaved with shaving cream and cleaned with isopropyl alcohol and iodopovidone. The skin and the periosteum from the lambdoid to the frontonasal sutures were removed, and muscles were partially detached from the skull to expose the occipital bone and the parietal ridges. To increase adherence of the implant to the skull, superficial grooves were drilled in the frontal, parietal, interparietal, and occipital bones. After leveling the skull yaw, pitch, and roll to obtain a flat skull configuration, two small reference crosses were scored using a scalpel at bregma and at the entry point of the Neuropixels probe (AP: 2.0/2.1 mm; ML: -2.0/-2.1 mm from bregma), and the incisions were filled with surgical ink and covered with UV-curable acrylic (Optibond). Finally, a titanium headplate was mounted onto the arm of the stereotaxic manipulator and attached to the skull with cyanoacrylate (Loctite 454) and dental cement (Paladur). Mice were allowed to recover in their home cages for at least 48 hours before being habituated to the experimental rig.

Habituation to the experimental rig

Mice were habituated to head-fixation and the experimental rig starting five days before the experiment. Three habituation sessions of increasing duration (20, 40, and 60 min) were run over consecutive days. During the familiarization and the recording sessions, the mouse sat inside a 3-D printed black plastic tube, leaving exposed only the head. A custom-made polyether ether ketone (PEEK) nose cone was

positioned in front of the mouse loosely fitting the mouse's snout. The nose cone was used to record the breathing signal and deliver the odorants during the experiments.

Craniotomies

Mice were anesthetized again and placed in the stereotaxic manipulator two days before the recording. Two small craniotomies were opened: one for probe insertion (AP: 2.0/2.1 mm; ML: -2.0/-2.1 mm from bregma) and the other over the contralateral posterior parietal cortex for the ground electrode. The dura mater was not removed. Finally, the two craniotomies were filled with surgical silicone (Kwik-Cast, WPI).

Tracheostomy

To probe PCx responses to the mechanical stimulation of the nasal cavity, we resorted to artificial ventilation. The electrophysiological recordings were performed immediately after the surgical preparation. For this procedure, mice were kept anesthetized throughout the surgical procedure and the recording with urethane (0.9 g/kg). Following a previously developed method (Eiting TP and Wachowiak M, 2018, https://bio-protocol.org/pdf/Bio-protocol3024.pdf), we placed a cannula into the nasopharynx via the upper part of the trachea to allow the artificial suction of air through the nasal cavity; another cannula was placed in the lower end of the trachea to allow the natural gas exchange with the lungs.

Bulbectomy

A craniotomy was opened above the OBs. Next, a blunted needle connected to a vacuum system was used to aspirate both OBs while applying a steady flow of Ringer's solution over the craniotomy until the cribriform plate was thoroughly cleaned and all the olfactory nerves were removed. Finally, the emptied cavity was filled with sterile gelatin sponge (Gelfoam) and covered with dental cement.

Stereotaxic probe insertion

All recordings were performed using Neuropixels 1.0 probes except for the TeLC experiments, where Neuronexus 32-channel silicon probes (A32-BuzsakiL) were used. The probe was mounted to a dovetail and affixed to a steel rod held by a micromanipulator (Luigs and Neumann). Before insertion, the back of the probe was coated with a solution of DiI (Thermofisher) using a paintbrush. Next, the silicone plug was removed from the craniotomies, and the probe was positioned above the recording site craniotomy (AP: 2.0/2.1 mm; ML: -2.0/-2.1 mm from bregma). Next, the probe was advanced through the dura and the cortex at approximately 5 μm/s until reaching the PCx (DV: 5.2/5.5 mm from bregma). The exact position depended on identifying a region with high firing rates and breathing-coupled activity. Then, the probe was retracted by 100 μm to allow the brain tissue to settle for 30 minutes before starting the recording. An Ag/AgCl electrode placed over the contralateral posterior parietal cortex was used for grounding. After electrode insertion, craniotomies were covered with a drop of agar solution (1% in Ringer's solution). Neuropixels data were acquired and recorded at 30 kHz through a PIXe interface

board connected to a PC. A32-BuzsakiL probe data were acquired and recorded at 30 kHz through an RHD2000 Series Intan board connected to a PC.

Experimental signals

Four signals were acquired besides the neural data: (1) a breathing signal generated by a flow sensor (AWM300V Honeywell) plugged into the nose cone; (2) an odor signal generated by a photo-ionization detector (200B miniPID, Aurora) that sampled the odorant inside the nose cone; (3) a TTL signaling the start of each odor trial and (4) a TTL signal generated by a Bpod Analog Input module (Sanworks) at the start of each inhalation. To identify the onset of an inhalation on-line, the breathing signal was fed into the Bpod Analog Input module, and a threshold was set at the breathing signal zero-crossing before the inhalation peak. All signals were digitized and recorded at 30 kHz using an Intan RHD2000 board. Finally, to align the neural data with the other signals, a 1 Hz TTL clock signal (50% duty cycle) or a barcode was generated by an Arduino One board and recorded by the PIXe board and the Intan board.

Odor delivery

Odorant stimuli were delivered using 5 seconds of odorant pulses. Odorants were delivered in 16 blocks (trials). The order of the odorants was randomized within each block. The inter-stimulus interval was randomly drawn from an exponential distribution (mean: 40 s, min-max: 30-50 s).

Odorants were delivered using a custom-made Arduino-controlled 13-valve olfactometer that delivers up to 12 odorants separately. The 13th valve was used to deliver a blank stimulus (no odor) between odor presentations. Odorants were contained in 15 ml vials partially filled with glass beads (Sigma-Aldrich). The headspace and the volume of odorant inside the vial were chosen to ensure that the amount of odor delivered within and across trials was steady as assessed by PID measurements. Each vial was separately connected to an olfactometer valve through a 3 in.-long PTFE tubing. Custom Arduino software-controlled valve opening and closing, enabling switching between odor vials and blank vial. At the beginning of a trial, the opening of an odor valve was synchronized with the onset of inhalation, as detected by the Bpod Analog Input Module.

Two streams of carbon-filtered air (F1 and F2) were independently routed to the nose cone at 1 l/min. The F1 stream consisted in odor (F1O; 0.1 l/min) and carrier (F1C; 0.9 l/min) streams mixed. Upon opening an odorant valve, the F1O flow was routed through the open vial to a PEEK manifold using a 3 in.-long PTFE tubing. Inside the manifold, the F1O flow from the open vial was mixed with the F1C flow to obtain the F1 airflow. The outlet of the mixing manifold was connected through a 0.5-in.-long PTFE tubing to a final three-way valve (V1). The F2 stream was directly connected to a second three-way solenoid valve (V2). The V1 and V2 valve outlets converged in a final 0.5 in. PTFE tubing connected to the nose cone. The F1 and F2 airflows reached the odor cone during odor-ON and odor-OFF epochs, respectively. The V1 outlet was open during the odor-ON epoch, whereas the V2 outlet was open during the odor-OFF epoch. At the beginning of a trial, the olfactometer opened the odor vial valve to load the tubing with odorized air up to the final valve V1, which diverted the flow outside the nose cone. After 2 seconds, the onset of an inhalation triggered an “odor-ON” TTL that switched the outlet opening of the V1 and V2 valves such that only the odorized airflow F1 entered now the nose cone. After 5 seconds

from the odor-ON TTL, the odor vial valve closed. After 10 seconds from closing of the odorant vial valve, the V1 and V2 valves were switched to the odor-OFF configuration.

The odor panel included two odors (pinene and eucalyptol) delivered at three concentrations (0.01, 0.1, and 1% v./v.), three odors (limonene, p-cymene, and methyl butyrate) delivered at two concentrations (0.01 and 1% v./v.) and four odors (eugenol, dicycloexyl disulfide, *p*-cymene, and methyl 2-furoate) delivered at a single concentration (0.01%). All odors were purchased from Sigma-Aldrich. To determine the dilution of each odor, a calibration curve was generated. To this aim, the signal generated by a photo-ionization detector (200B miniPID, Aurora) upon delivery of an odor at three dilutions (no dilution, 1:8, and 1:160 in mineral oil, Sigma-Aldrich; 10 presentations per dilution) was recorded. Then, an exponential curve was fitted to the miniPID traces to obtain the coefficient A for each dilution. Next, a second-order polynomial was fitted to the three A coefficients of each odor. Finally, the dilutions corresponding to 0.1%, 1%, and 10% v./v. of undiluted odor were extrapolated from the fitted polynomial. The carrier airflow further diluted the odor concentration by 10 to reach the final concentration of 0,01, 0.1, and 1 % v./v. After entering inside the nose mask through a lateral port, odors were actively extracted using a vacuum line attached to a port on the opposite side of the mask.

Artificial stimulation of the nasal cavity

The cannula in the nasopharynx was attached to a computer-controlled solenoid valve which was connected to a vacuum line. The opening of the valve drew air inside the nasal cavity. The air was deodorized through a carbon filter before entering the nose cone. We applied 150-ms pulses of suction at 750-ms intervals. We tested five flow rates that span the range of estimated nasal flow rates in mice (50, 100, 150, 200, and 250 ml/min).

Histology

Mice were deeply anesthetized with 1 g/kg urethane injection and intracardially perfused with 1% phosphate buffer solution (PBS) followed by 4% paraformaldehyde (PFA). The brain was dissected and immersed in 4% PFA for 24 h. Following fixation, the brain was washed with PBS and sectioned coronally (80 µm) with a vibratome. Sections were counter-stained with DAPI, and images were acquired with a fluorescence microscope at 10x magnification. The Allen CCF open-source toolbox was used to reconstruct the probe location in 3D (https://github.com/cortex-lab/allenCCF).

Analysis of the breathing signal

The breathing signal was bandpass filtered between 0.5 to 50Hz using the MATLAB FMAToolbox (http://fmatoolbox.sourceforge.net/) and smoothed with a Gaussian kernel (standard deviation: 25 ms). Inhalation peaks were identified as the local minima of the respiratory signal. Inhalation peaks closer than 65 ms from the next peak were discarded. Inhalation onset and offset were identified as the breathing signal zero-crossings before and after the inhalation peak. Inhalation length was defined as the difference between the inhalation offset and onset times. The breathing cycle was calculated as the difference between two consecutive inhalation onsets. The negative inhalation slope was defined as the

slope of the line between the nearest two points before the inhalation peak in the z-scored respiration signal with a value equal to 10% and 90% of the inhalation peak amplitude. Similarly, the positive inhalation slope was calculated as the slope of the line between the 90% to 10% of inhalation amplitude points in the z-scored respiration signal after the inhalation peak.

Inhalation clustering

Inhalation waveforms were isolated by extracting the breathing signal within a 100 ms-long window centered on the inhalation peak. Each waveform was normalized by its 2-norm and considered as a point in a high-dimensional space. The dimensionality of the inhalation space was reduced by applying PCA using the *'pca'* function in MATLAB (Mathworks; Extended Data Fig. 1B). The projection of the inhalation vector onto the *n*-dimensional subspace spanned by the *n* first PCs (where *n* is the minimum number of PCs that explain at least 98% of total variance) was calculated. The inhalation vectors in the *n*-dimensional space were clustered with a Gaussian Mixture Model using the *'fitgmdist'* function in MATLAB (Mathworks; maximum number of iterations: 10,000, regularization value: 0.05, replicates: 15, full covariance matrix). The Calinski-Harabasz index was used to determine the optimal number of clusters. The centroid vector for each cluster was defined as the mean vector of all inhalation vectors within the cluster. To consolidate the GMM clustering, a Hierarchical Cluster (HC) dendrogram was applied to the centroid vectors using the *'linkage'* function in MATLAB (distance metric: correlation). The HC dendrogram from an individual experiment usually resulted in two or three clusters. Visual inspection of the dendrograms suggested two clusters were similar and stemmed from the same branch; thus, we merged the two clusters with the same parent. Finally, we assigned the clusters to the "slow" and "fast" inhalation types based on the mean of the inhalation lengths within each cluster, with "fast" inhalation assigned to the class with smaller inhalation lengths. The clustering algorithm was cross-validated on the inhalations from eight mice by fitting the GMM on a training set consisting of all the inhalations from seven mice and then using the fitted model to predict the labels of the inhalations from the held-out mouse. The ground-truth inhalation labels for the held-out mouse were obtained using the above clustering pipeline. This process was repeated for all possible combinations of test and train sets, and the classification accuracies were finally averaged. This clustering pipeline classified the inhalation label of held-out inhalations with 98% accuracy.

Spike sorting and inclusion criteria

Spikes were sorted using KiloSort3 (https://github.com/MouseLand/Kilosort). All clusters were manually curated using Phy (https://github.com/cortex-lab/phy). During the manual curation process, the quality of every single unit assigned by the automatic sorting algorithm was evaluated based on several criteria, such as the violation of the refractory period, the firing rate, and the stability of the amplitude. Specifically, units that did not meet the quality criteria were removed from further analyses. Additionally, single units with a firing rate of less than 0.5 Hz were excluded from the subsequent analyses; this threshold was lowered to 0.1 Hz in the experiments with tracheostomized mice because the urethane anesthesia reduced the baseline firing rate.

Analysis of sniff-by-sniff responses

Inhalation and odor response were measured as the average spike count within a 70 or 180 ms window after the inhalation onset. Smoothed peri-inhalation time histograms (PITH) were obtained by convolving the spike-times series within an inhalation with a Gaussian kernel (standard deviation: 10 ms), then averaging across all inhalations of the same type and finally subtracting the average firing rate across the odor-free epochs of the entire recording session. Odorless-air inhalations were defined as those occurring within the -13 to -4 seconds window before the delivery of an odor. This window was considered sufficient to remove any lingering odor because the minimum time interval between two odor presentations was 30 s, and a vacuum line constantly exhausted odorants from the nose mask. Sniff-by-sniff odor responses were measured in a time window starting 400 ms after the odor onset and lasting for 4.6 s. The first two trials of each odor-concentration stimulus were excluded to avoid any bias due to the novelty of the stimulus. Furthermore, we excluded the first 400 ms of odor presentation because this period was dominated by fast sniffs (Extended Data Fig. 1B) and the typical transient response. Therefore, we did not analyze odor responses during the first inhalation of an odor. Although rodents can be trained to discriminate odor identity and concentration within the first couple of inhalations, our study was not meant to investigate sniff-invariant odor representations during a trained discrimination task.

Concentration discrimination index

To measure how well a neuron could discriminate two concentrations, we first computed an area-under-the-receiver-operating-curve (auROC) using the spike counts during the inhalation of 0.01 and 0.1% v./v. odorant. The CDI was computed as abs(1 - 2*auROC). To generate the spike count distribution for each concentration, a random sample of inhalations was taken during the presentation of that concentration; an equal sample size was used for the two concentrations. Next, three different CDI were calculated based on a sample of slow inhalations, fast inhalations, and mixed slow and fast inhalations; 100 samples were drawn for each set of inhalations and an average CDI was calculated for slow, fast and mixed inhalations.

Tuning curves

To obtain neural tuning curves during artificial stimulation of the nasal cavity, the average response for each airflow rate was calculated as the difference between the number of spikes fired by a neuron during the (0 500] and (-500 0] ms window where 0 is the onset of the air pulse

To obtain neural tuning curves during natural breathing, inhalations were sorted into ten quantile bins based on the amplitude of the peak of airflow as measured by the flow sensor. This was done to ensure that each bin contained an equal number of inhalations. The tuning curve was generated by using the average response to an odorless inhalation during the first 180 ms for each bin.

Tuning curves were z-scored, and their slopes were calculated by linearly regressing the neural response to the airflow rate.

Encoding models

A Poisson Generalized linear model (GLM) with regularization was employed to estimate the contribution of inhalation dynamics, odor concentration, and their interaction with the sniff-by-sniff odor response of a neuron. The GLM was fitted using the glmnet toolbox (https://hastie.su.domains/glmnet_matlab/) in MATLAB (Mathworks) with elastic net regularization, where the parameter *alpha* controlled elastic net penalty. A value of 0.95 was used for *alpha*, which smoothly interpolates the gap between lasso (*alpha* = 0) and ridge regression (*alpha* = 1). The optimal elastic net penalty value was selected using a 10-fold cross-validation approach.

The conclusions from the GLM analysis were confirmed using a linear regression model. In this case, the normalized firing rate r_i of neuron *i* during the first 70 or 180 ms of an inhalation was modeled with the following equation:

$$z\ score\ (r_i) = \alpha_i I + \beta_i C + r_{0i} + \eta$$

Here, the *I* term represents the inhalation dynamics (0 for slow and 1 for fast), and the *C* term represents the odor concentration (varying from 0 to 1 based on the logarithm of the concentration). The term r_0 is a baseline bias, and η is a Gaussian noise term. Next, the residual of r_i, $\tilde{r_i}$, was calculated to assess whether the mechanosensory and olfactory components of the neuron's response interacted. The residual was then fitted with a model with a single interaction term:

$$\tilde{r_i} = z\ score\ (r_i) - \alpha_i I - \beta_i C - r_{0i}$$
$$\tilde{r_i} = \gamma_i IC + \eta$$

Where *IC* represents the interaction between the mechanosensory and olfactory factors of the neuron's response, and η represents a Gaussian noise term. To fit the models, inhalations were randomly sampled from all inhalations to have an equal size for each combination of inhalation speed and odor concentration term. The vector of the neural responses to the inhalations was z-scored and passed to the model with the corresponding design matrix. The significance of the model's coefficients was assessed using an ANOVA test. The random sampling was repeated 100 times, and the coefficients of each term and their p-values were averaged across all re-samplings.

Orthogonal representations in heterogeneous mixed-selectivity codes

Heterogeneous mixed selectivity of neural responses has an immediate connection with orthogonality of population representations. This can be seen in a simple model, as follows. Consider a population code similar to the one described above, where the firing rate r_i of cell i is

$$r_i = r_0 + \alpha_i I + \beta_i C + \gamma_i I C$$

where, as above, I is the inhalation speed, and C is the concentration. For a population of size N ($1 \leq i \leq N$), we can also write this in vector form as

$$r = r + \alpha I + \beta C + \gamma I C$$

where r, α, β, and γ are now vectors with N entries. Assume that the number N of neurons is large and that coding is heterogeneous (that is, there is no special structure to the code), so that α, β, and γ are random vectors in N dimensions. In this case, α can be thought of as a scalar $|\alpha|$ controlling the overall intensity of tuning for inhalation speed in the population, times a random vector on the unit sphere, and the same for β and γ**.** The direction along which the population vector r encodes the concentration is

$$\frac{dr}{dC} = \beta + \gamma I$$

In other words, the concentration C is encoded in the direction β for slow inhalation (I=0) and the direction $\beta + \gamma$ for fast inhalation (I=1). The cosine of the angle θ between the two encoding directions is

$$\cos(\theta) = \frac{<\beta, \beta + \gamma>}{|\beta| \cdot |\beta + \gamma|} = \frac{|\beta|^2 + <\beta, \gamma>}{|\beta|\sqrt{|\beta|^2 + |\gamma|^2 + 2 <\beta, \gamma>}}$$

However, if β and γ are high-dimensional and their direction is chosen at random, we can assume they are approximately orthogonal (Cai, Tony, Jianqing Fan, and Tiefeng Jiang. "Distributions of Angles in Random Packing on Spheres," *Journal of Machine Learning Research* 14 (2013) 1837-1864), and $<\beta,\gamma> \approx 0$. Accordingly,

$$\cos(\theta) \approx \frac{|\beta|^2}{|\beta|\sqrt{|\beta|^2 + |\gamma|^2}} = \frac{|\beta|}{\sqrt{|\beta|^2 + |\gamma|^2}}$$

Therefore, the concentration encoding directions will tend towards orthogonality in the presence of strong interactions (when $\gamma >> \beta$, $\cos(\theta)=0$) and will be parallel when interactions are absent or weak (when $|\gamma|=0$, $\cos(\theta)=1$).

Pseudo-population response matrix generation

The pseudo-population response matrix was obtained by pooling all recorded neurons' sniff-by-sniff spike count responses to the inhalation events from all animals within the same experimental design. To create this matrix, an equal number of inhalation events for each odor concentration was randomly drawn from all inhalation events of all mice. Half of these events were fast inhalations, and the other half were slow inhalations. This allowed for an equal representation of both inhalation types in the sample. The same number of inhalations was sampled for each concentration, and then all inhalations were pooled. The response of each neuron to each inhalation in the selected sample was then vertically

concatenated to obtain a population response vector during an inhalation. Finally, the response vectors of all neurons were concatenated horizontally to create a pseudo-population response matrix.

PCA embeddings

To visualize the neural representation of odor concentrations across different inhalation dynamics, PCA analysis was performed on the response covariance matrices obtained from a neural pseudo-population or single mouse neural populations. Before applying PCA, the neural responses of individual neurons were z-scored. PCA was also used to determine the projections onto the first 15 PCs of the sniff-by-sniff responses; these projections were separately used to decode inhalation dynamics in Fig. 5B and Extended Data Fig. 5B and odor concentration and identity in Fig. 5B, D and Extended Data Fig. 5B-F.

Analysis of the angle between the concentration and the inhalation encoding axes

The encoding direction for odor concentrations and inhalation dynamics was determined using concentration-encoding unit vectors and sampling-encoding unit vectors; these two vectors were defined as unit vectors in the sniff-by-sniff response space. Linear discriminant analysis (LDA) was used to calculate the encoding vectors. Specifically, a pseudo-population response matrix with corresponding labels for each odor concentration and inhalation dynamics was used to fit the LDA model. This operation was performed using the Python scikit-learn library. The eigenvalue decomposition solver was used to fit the LDA model with a shrinkage parameter that was automatically calculated by the Ledoit-Wolf lemma algorithm. The encoding vector was taken as the first column of the LDA transform scaling matrix. For each inhalation speed, the concentration-encoding unit vector was obtained from the LDA fit by using a pseudo-population response during a given inhalation dynamics and concentration using a different label for each concentration. Similarly, the inhalation-encoding unit vector was obtained from the LDA fit using pseudo-population response during either inhalation dynamics, and the type of inhalation dynamics was used as a label. Finally, the average angle between the concentration-encoding vectors for each inhalation dynamics and the average angle Θ between the concentration-encoding vectors and inhalation-encoding vectors were calculated and then transformed as: $\Theta' = 90 - |90 - \Theta|$. This procedure was repeated 100 times with pseudo-population response matrices built using different randomly sampled neurons for each run.

Inhalation dynamics decoding analysis

A linear support vector machine (lSVM) classifier was utilized for all classification analyses (inhalation dynamics, odor concentration, odor identity, and generalization analysis). The lSVM was implemented using the MATLAB (Mathworks) NDT (http://www.readout.info/ndt-version-1-0-4-is-released/) and libsvm (http://www.csie.ntu.edu.tw/~cjlin/libsvm/) toolbox. A 10-fold cross-validation was performed for all models. Before model fitting, the sniff-by-sniff neural responses in the training and test set were separately z-scored.

To decode the inhalation dynamics, a pseudo-population response matrix was generated using only the spike counts during 70 or 180 ms windows for each inhalation of odorless air. Specifically, 400 random slow and fast inhalations were drawn, and the spike counts in 70 or 180 ms windows were used to build

the response matrix of a pseudopopulation or an individual mouse population. The decoding accuracy for different numbers of neurons was determined by drawing random subsamples of neurons of different numerosity. This resampling process was repeated 100 times for each number of neurons to obtain reliable estimates of decoding accuracy. Additionally, the entire classification process was repeated 100 times, randomizing the sampled inhalation events included in each run. The reported accuracy for each number of neurons represents the mean of all resampling processes.

Concentration decoding analysis

To classify odor concentration (0.01, 0.1, and 1% v./v.), a pseudo-population response matrix or a single animal population response matrix was built using the same number of inhalations for each odor-concentration pair to avoid any potential bias due to different inhalation sample sizes. Next, for each odor, corresponding rows of this matrix or its PC projections were sorted and passed to the classifier to decode the concentration in either the whole population response space or its PC projections space. This procedure was repeated 100 times with pseudo-population response matrices with different randomly sampled inhalations. The reported accuracies are the mean and standard deviation across all resampling processes.

To investigate the geometry of the neural space, a generalization paradigm was employed. To this end, a lSVM trained on data from one inhalation dynamics was tested on data from the other inhalation dynamics (*trans*-decoder). The average accuracy of *trans*-decoders was compared to that of *cis*-decoders that had been trained and tested instead on the odor responses during the same inhalation dynamics.

To assess the importance of heterogeneous selectivity for mechanosensory and olfactory inputs for sniff-invariant odor representations, we first fit the sniff-by-sniff responses of individual neurons with a linear regression model including a concentration (C = 0.01, 0.1, and 1%) and an inhalation dynamics (slow: I = 0; fast: I = 1) regressor. Then we selected a sub-pseudo-population with highly correlated mechanosensory (α) and olfactory regressor coefficients (β). To this end, a sub-pseudo-population of neurons meeting the following conditions were considered positively correlated: ($|\beta| >= |\alpha*\tan(pi/12)|$) and ($|\beta| <= |\alpha*\tan(5*pi/12)|$) with α and β having the same sign. Finally, another subset of neurons with α and β having different signs was selected to build a sub-pseudo-population with negatively correlated mechanosensory and concentration regressors. The union of these two sets was considered as the uncorrelated sub-pseudo-population. Then, an equal number of neurons was randomly sampled from these three sub-pseudo-populations, and their sniff-by-sniff odor responses were used by *cis*- and *trans*-decoders.

Inhalation phase decoding

To predict the inhalation phase from neuronal activity, we employed a Support Vector Regression (SVR).

Preprocessing. First, the firing rate for every neuron was computed using a rolling gaussian window with sd = 20 ms (gaussian_filter() from scipy.ndimage). The firing rate matrix and the respiration trace were then downsampled to 10 ms bins to speed up the following computations. For every animal, the analysis was restricted to areas with at least 20 recorded neurons.

Inhalation phase. Analysis was restricted to the inhalation events defined and classified as described in the section *Inhalation clustering*. The inhalation phase was a number in the interval [0, 1] where 0 and 1 corresponded to the beginning and the end of the inhalation event, and the other values were linearly interpolated.
PCA decomposition. First, neuronal activity from all the neurons of each area was projected over principal components using the PCA class from sklearn.decomposition. To focus on the most relevant components for the prediction, PCs up to a cumulative explained (relative) variance > 0.5 were included (at least two PCs were always selected). We note that the analysis results hold for different inclusion criteria for the number of PCs.
Epochs definition. For the training and testing of the model, suitable non-overlapping epochs were created by concatenating inhalation periods for a total duration of 30 s. Depending on the inhalation number and classification, this resulted in a variable number of epochs (between 2 and 4) for every experimental animal. For every animal, all permutations of pairs of those suitable epochs were used as test and training datasets. Results were robust to different choices of epochs (i.e., more epochs with shorter windows).
SVR training. An SVR model was trained using SVR from sklearn.svm(), and its default parameters (kernel = 'rbf', degree = 3, gamma = 'scale', coef0 = 0.0, tol = 0.001, C = 1.0, epsilon = 0.1, shrinking = True; where 'rbf' kernel is the Radial Basis Function, and 'scale' gamma is 1 / (n_features * X.var())). The source data was the (n_components, timepoints) array of PC data; the variable to predict was the (timepoints,) array of inhalation phase data. The shuffle distributions were calculated by randomizing the inhalation phase array before prediction.
Evaluation. For every permutation of the epochs, the inhalation phase was predicted at every time point, and the performance of the model was assessed by calculating the squared Pearson correlation between the ground truth and the predicted data and then averaged across permutations.

Decoding of concentration over time and phase bins
Feature vectors generation. First, we generated time- and phase-binned vectors of neuronal activity after the inhalation onset as follows:

- Time-binned vectors of 180 ms: the firing rate traces of all neurons in an area were used, as defined in the above section *Decoding of the inhalation phase. Preprocessing.* The traces were cropped from the onset of each inhalation in a 180 ms window and binned in 10-ms bins. Then, the traces of all neurons were concatenated to obtain, for every inhalation, an array with size (n_timebins x n_neurons), with n_timebins = 18.
- One-bin time vectors: the time-binned arrays defined above were averaged over the time bins.
- Time-binned vectors cropped over a full inhalation cycle: the respiratory phase was computed using the Hilbert transform. The time window in which the respiratory phase increased by 2π was found for every inhalation. Then, the firing rate trace was cropped in this window, padding it with zeros to account for the different durations of each inhalation period to a total of 500 ms (enough to accommodate > 99% of all inhalations). The arrays were then binned in 10-ms bins

and concatenated across neurons to a total of (n_timebins x n_neurons) for every inhalation, with n_timebins = 50.

- Phase-binned vectors: the respiratory phase was computed using the Hilbert transform. The time window in which the respiratory phase increased by 2π was found for every inhalation. The firing rate trace was cropped in this window and then binned into 36 bins equally spaced in phase. In this way, no zero-padding was necessary. Next, the activity of all neurons was concatenated to obtain an array with length (n_phasebins x n_neurons) for every inhalation, with n_phasebins = 36 and zero-padding at the end to ensure array length consistency.

Odor concentration decoding. To decode odor concentration from the firing rates, we used an SVM classifier using a generalization procedure like the one described above. First, inhalations were sampled 100 times with replacement for every animal to obtain a consistent number of events for each combination (inhalation_type, concentration). Then, ten-fold validation was used for training and testing the classifier for each extraction. Data were split into ten blocks, and the SVM trained over nine blocks and tested over the remaining one iterating over all ten possible left-out blocks. The SVM model was trained using SVC from sklearn.svm, and its default parameters but for the linearity of the kernel (kernel = linear, gamma = 'scale', coef0 = 0.0, tol = 0.001, C = 1.0, epsilon = 0.1, shrinking = True; where 'scale' gamma is 1/(n_features * X.var())). The source data was the ((n_bins x n_neurons), n_inhalations) array of concatenated firing rates over time for each inhalation; the variable to predict was the (n_inhalations) array of concentrations presented during each inhalation. For each iteration, the SVM was evaluated by computing the fraction of correct predictions. This number was then averaged across all folds and samplings (1000 different classifications) to obtain the numbers reported in the figures. Finally, the analysis was repeated separately for the two presented odors, and the results eventually merged.

Simulation of neural responses with varying levels of inhalation-dependent concentration change

We tested whether integrating odor-independent mechanosensory inputs in the PCx code offsets the odor concentration alteration (ΔIC) inside the nasal cavity due to changes in inhalation dynamics. To this end, we compared odor concentration decoding using the pattern activity of two simulated populations of neurons with or without mechanosensory inputs. We reasoned that the ΔIC should be proportional to the external concentration and additive. Thus, we simulated the sniff-by-sniff responses of each neuron using the following Poisson model:

$$R_j = \text{Poiss}\left(a_j \, \text{I} + \beta_j \, C_n \right), \qquad with \;\; C_n = \log(\text{C}_e + \text{k I C}_e)$$

R_j is the simulated neural response during a sniff. a_j and β_j are the mechanosensory and olfactory regressor coefficients previously estimated using a linear regression model fitted to the actual responses of neuron *j*. I is equal to 0 for slow inhalations and 1 for fast inhalations. C_e is the external odor concentration (0.01, 0.1, and 1%). k is a proportional factor that was parametrically changed in the range between 0 and 1 to simulate different levels of ΔIC; k = 0 means that a slow-to-fast change in inhalation dynamics does not change the odorant concentration (ΔIC = 0), whereas k = 1 means that a slow-to-fast change in inhalation dynamics increases the odor concentration inside the naris by 100% of the external

concentration ($\Delta IC = C_e$). The population of neurons without mechanosensory inputs was generated by setting α to 0. α was set to 0 to simulate the population of neurons without mechanosensory inputs.

V1 data analysis

To extend our analysis to the visual system, we used the open dataset shared by the Allen Brain Institute under the Brain Observatory Project (Siegle et al., 2021 https://www.nature.com/articles/s41586-020-03171-x). All the Neuropixel experiments with pupillometry data in the "Functional_connectivity" dataset were downloaded using the AllenSDK, v 2.13.9. We restricted the analysis to the data recorded during the "Contrast tuning" block. In this block, a whole-screen sinusoidal pattern of different orientations and drifting in four different directions [90°, 45°, 90°, 135°; clockwise from 0° vertical] was presented at nine different, logarithmically scaled contrast levels between 1% and 100% of the monitor contrast range. Finally, we restricted our analysis to the responses to the drifting gratings with 0° orientation. The temporal frequency of the gratings was 2 Hz, and the spatial frequency was 0.04 cycles/degree. For a complete description of the visual stimulus presentation, see the technical white paper available at the Allen Brain website (https://brainmapportal-live-4cc80a57cd6e400d854-f7fdcae.divio-media.net/filer_public/80/75/8075a100-ca64-429a-b39a-569121b612b2/neuropixels_visual_coding_-_white_paper_v10.pdf).

We averaged the pupil_height and pupil_width variables provided in the dataset to estimate the pupil size. Then, we assigned the pupil sizes at each time point to the "small" or "large" class based on whether the pupil was larger or smaller than the median computed over the whole experiment. The results did not change if we used a finer binning of the pupil sizes. We did not control for the locomotion speed of the animal because we were only interested in the relationship between non-visual and visual inputs and the pupil-size-invariance of contrast encoding regardless of the actual source of the non-visual input.

We used the AllenSDK interface to extract the spike count during the stimulus presentation. Each visual stimulus lasted 500 ms. The downloaded database included 23 experiments and 1496 primary visual cortex (VISp) units. We finally selected 1085 VISp units from 18 experiments (767871931, 771990200, 778240327, 778998620, 781842082, 786091066, 787025148, 789848216, 793224716, 794812542, 816200189, 819186360, 819701982, 821695405, 829720705, 839068429, 839557629, 847657808) because these experiments had enough big and small pupil size events to run our encoding and decoding analysis.

Statistical tests

The Student's t-test (two-sided) was used to compare two normal independent distributions. For comparing two independent distributions when normality cannot be assumed, significance was assessed by permutation testing or using the Wilcoxon Rank Sum test (two-sided). For regression modeling, confidence intervals are computed over bootstraps (with replacement) of the data.

REFERENCES

1. Crapse TB, Sommer MA. Corollary discharge across the animal kingdom. *Nat Rev Neurosci*. 2008;9(8):587-600. doi:10.1038/nrn2457
2. von Holst E, Mittelstaedt H. The principle of reafference: Interactions between the central nervous system and the periphery. *Science (80-)*. 1950;37(20):464-476.
3. Sherrington CS. Observations on the sensual role of the proprioceptive nerve supply of the extrinsic ocular muscles. *Brain*. 1918;41(3-4):332-343. doi:10.1093/brain/41.3-4.332
4. Teghtsoonian R, Teghtsoonian M, Berglund B, Berglund U. Invariance of odor strength with sniff vigor: an olfactory analogue to size constancy. *J Exp Psychol Hum Percept Perform*. 1978;4(1):144-152. doi:10.1037//0096-1523.4.1.144
5. Mainland JD, Sobel N. The sniff is part of the olfactory percept. *Chem Senses*. 2006. doi:10.1093/chemse/bjj012
6. Kepecs A, Uchida N, Mainen ZF. The sniff as a unit of olfactory processing. *Chem Senses*. 2006;31(2):167-179. doi:10.1093/chemse/bjj016
7. Catania KC. Stereo and serial sniffing guide navigation to an odour source in a mammal. *Nat Commun*. 2013;4. doi:10.1038/ncomms2444
8. Parabucki A, Bizer A, Morris G, et al. Odor concentration change coding in the olfactory bulb. *eNeuro*. 2019;6(1):1-13. doi:10.1523/ENEURO.0396-18.2019
9. Findley TM, Wyrick D, Cramer JL, et al. Sniff-synchronized, gradient-guided olfactory search by freely moving mice. *Elife*. 2021. doi:10.7554/elife.58523
10. Wachowiak M. All in a Sniff: Olfaction as a Model for Active Sensing. *Neuron*. 2011. doi:10.1016/j.neuron.2011.08.030
11. Wesson DW, Donahou TN, Johnson MO, Wachowiak M. Sniffing behavior of mice during performance in odor-guided tasks. *Chem Senses*. 2008;33(7):581-596. doi:10.1093/chemse/bjn029
12. Youngentob SL, Mozell MM, Sheehe PR, Hornung DE. A quantitative analysis of sniffing strategies in rats performing odor detection tasks. *Physiol Behav*. 1987;41(1):59-69. doi:10.1016/0031-9384(87)90131-4
13. Schoenfeld TA, Cleland TA. Anatomical contributions to odorant sampling and representation in rodents: Zoning in on sniffing behavior. *Chem Senses*. 2006;31(2):131-144. doi:10.1093/chemse/bjj015
14. Mozell MM, Jagodowicz M. Chromatographic Separation of Odorants by the Nose : Retention Times Measured across in vivo Olfactory Mucosa Author (s): Maxwell M . Mozell and Morris Jagodowicz Published by : American Association for the Advancement of Science Stable URL : https://ww. 1973;181(4106):1247-1249.
15. Kent PF, Mozell MM, Murphy SJ, Hornung DE. The interaction of imposed and inherent olfactory mucosal activity patterns and their composite representation in a mammalian species using voltage-sensitive dyes. *J Neurosci Off J Soc Neurosci*. 1996;16(1):345-353. doi:10.1523/JNEUROSCI.16-01-00345.1996
16. Grosmaitre X, Santarelli LC, Tan J, Tan J, Luo M, Ma M. Dual functions of mammalian olfactory sensory neurons as odor detectors and mechanical sensors. *Nat Neurosci*. 2007. doi:10.1038/nn1856

17. Connelly T, Yu Y, Grosmaitre X, et al. G protein-coupled odorant receptors underlie mechanosensitivity in mammalian olfactory sensory neurons. *Proc Natl Acad Sci U S A*. 2015. doi:10.1073/pnas.1418515112
18. Mozell MM, Kent PF, Murphy SJ. The effect of flow rate upon the magnitude of the olfactory response differs for different odorants. *Chem Senses*. 1992;17(3):361. doi:10.1093/chemse/17.3.361
19. Cenier T, McGann JP, Tsuno Y, Verhagen J V, Wachowiak M. Testing the Sorption Hypothesis in Olfaction: A Limited Role for Sniff Strength in Shaping Primary Odor Representations During Behavior. *J Neurosci*. 2013;33(1):79 LP - 92. doi:10.1523/JNEUROSCI.4101-12.2013
20. Shusterman R, Sirotin YB, Smear MC, Ahmadian Y, Rinberg D. Sniff invariant odor coding. *bioRxiv*. 2017. doi:10.1101/174417
21. Jordan R, Jordan R, Jordan R, et al. Sniffing Fast: Paradoxical Effects on Odor Concentration Discrimination at the Levels of Olfactory Bulb Output and Behavior. *eNeuro*. 2018. doi:10.1523/eneuro.0148-18.2018
22. Wesson DW, Verhagen J V, Wachowiak M. Why sniff fast? The relationship between sniff frequency, odor discrimination, and receptor neuron activation in the rat. *J Neurophysiol*. 2009. doi:10.1152/jn.90981.2008
23. Carey RM, Wachowiak M. Effect of Sniffing on the Temporal Structure of Mitral/Tufted Cell Output from the Olfactory Bulb. *J Neurosci*. 2011. doi:10.1523/jneurosci.1805-11.2011
24. Shusterman R, Smear MC, Koulakov AA, Rinberg D. Precise olfactory responses tile the sniff cycle. *Nat Neurosci*. 2011. doi:10.1038/nn.2877
25. Díaz-Quesada M, Youngstrom IA, Tsuno Y, Hansen KR, Economo MN, Wachowiak M. Inhalation Frequency Controls Reformatting of Mitral/Tufted Cell Odor Representations in the Olfactory Bulb. *J Neurosci*. 2018;38(9):2189 LP - 2206. doi:10.1523/JNEUROSCI.0714-17.2018
26. Bathellier B, Buhl DL, Buhl DL, Accolla R, Carleton A. Dynamic Ensemble Odor Coding in the Mammalian Olfactory Bulb: Sensory Information at Different Timescales. *Neuron*. 2008. doi:10.1016/j.neuron.2008.02.011
27. Bolding KA, Franks K, Franks KM. Complementary codes for odor identity and intensity in olfactory cortex. *Elife*. 2017. doi:10.7554/elife.22630
28. Pashkovski SL, Iurilli G, Brann DH, et al. Structure and flexibility in cortical representations of odour space. *Nature*. 2020. doi:10.1038/s41586-020-2451-1
29. Iurilli G, Datta SR. Population Coding in an Innately Relevant Olfactory Area. *Neuron*. 2017;93(5). doi:10.1016/j.neuron.2017.02.010
30. Fontanini A, Spano P, Bower JM. Ketamine-Xylazine-Induced Slow (< 1.5 Hz) Oscillations in the Rat Piriform (Olfactory) Cortex Are Functionally Correlated with Respiration. *J Neurosci*. 2003. doi:10.1523/jneurosci.23-22-07993.2003
31. Poo C, Isaacson JS. Odor representations in olfactory cortex: "sparse" coding, global inhibition, and oscillations. *Neuron*. 2009. doi:10.1016/j.neuron.2009.05.022
32. Sobel N, Prabhakaran V, Desmond JE, et al. Sniffing and smelling: separate subsystems in the human olfactory cortex . *Nature*. 1998;392(6673):282-286. doi:10.1038/32654

33. Litaudon P, Amat C, Bertrand B, Vigouroux M, Buonviso N. Piriform cortex functional heterogeneity revealed by cellular responses to odours. *Eur J Neurosci*. 2003;17(11):2457-2461. doi:10.1046/j.1460-9568.2003.02654.x
34. Wilson DA. Odor specificity of habituation in the rat anterior piriform cortex. *J Neurophysiol*. 2000;83(1):139-145. doi:10.1152/jn.2000.83.1.139
35. Rennaker RL, Chen CFF, Chen C-FF, Ruyle AM, Sloan AM, Wilson DA. Spatial and Temporal Distribution of Odorant-Evoked Activity in the Piriform Cortex. *J Neurosci*. 2007. doi:10.1523/jneurosci.4072-06.2007
36. Kepecs A, Uchida N, Mainen ZF. Rapid and Precise Control of Sniffing During Olfactory Discrimination in Rats. *J Neurophysiol*. 2007. doi:10.1152/jn.00071.2007
37. Oka Y, Takai Y, Touhara K. Nasal Airflow Rate Affects the Sensitivity and Pattern of Glomerular Odorant Responses in the Mouse Olfactory Bulb. *J Neurosci*. 2009;29(39):12070 LP - 12078. doi:10.1523/JNEUROSCI.1415-09.2009
38. Verhagen J V, Wesson DW, Netoff TI, White JA, Wachowiak M. Sniffing controls an adaptive filter of sensory input to the olfactory bulb. *Nat Neurosci*. 2007. doi:10.1038/nn1892
39. Iwata R, Kiyonari H, Imai T. Mechanosensory-Based Phase Coding of Odor Identity in the Olfactory Bulb. *Neuron*. 2017;96(5):1139-1152.e7. doi:10.1016/j.neuron.2017.11.008
40. Bolding KA, Franks K, Franks KM. Recurrent cortical circuits implement concentration-invariant odor coding. *bioRxiv*. 2018. doi:10.1101/294132
41. Haddad R, Lanjuin A, Madisen L, Zeng H, Murthy VN, Uchida N. Olfactory cortical neurons read out a relative time code in the olfactory bulb. *Nat Neurosci*. 2013;16(7):949-957. doi:10.1038/nn.3407
42. Stringer C, Pachitariu M, Steinmetz N, Reddy CB, Carandini M, Harris KD. Spontaneous behaviors drive multidimensional, brainwide activity. *Science (80-)*. 2019;364(6437):eaav7893. doi:10.1126/science.aav7893
43. Miura SK, Scanziani M. Distinguishing externally from saccade-induced motion in visual cortex. *Nature*. 2022;610(7930):135-142. doi:10.1038/s41586-022-05196-w
44. Reimer J, Froudarakis E, Cadwell CR, Yatsenko D, Denfield GH, Tolias AS. Pupil Fluctuations Track Fast Switching of Cortical States during Quiet Wakefulness. *Neuron*. 2014;84(2):355-362. doi:10.1016/j.neuron.2014.09.033
45. Franke K, Willeke KF, Ponder K, et al. State-dependent pupil dilation rapidly shifts visual feature selectivity. *Nature*. 2022;610(7930):128-134. doi:10.1038/s41586-022-05270-3
46. Campbell FW, Gregory AH. Effect of Size of Pupil on Visual Acuity. *Nature*. 1960;187(4743):1121-1123. doi:10.1038/1871121c0
47. Laughlin SB. Retinal information capacity and the function of the pupil. *Ophthalmic Physiol Opt*. 1992;12(2):161-164. doi:https://doi.org/10.1111/j.1475-1313.1992.tb00281.x
48. Tikidji-Hamburyan A, Reinhard K, Seitter H, et al. Retinal output changes qualitatively with every change in ambient illuminance. *Nat Neurosci*. 2015;18(1):66-74. doi:10.1038/nn.3891
49. Bedell HE, Tong J, Aydin M. The perception of motion smear during eye and head movements. *Vision Res*. 2010;50(24):2692-2701. doi:10.1016/j.visres.2010.09.025

50. Vélez-Fort M, Bracey EF, Keshavarzi S, et al. A Circuit for Integration of Head- and Visual-Motion Signals in Layer 6 of Mouse Primary Visual Cortex. *Neuron*. 2018;98(1):179-191.e6. doi:https://doi.org/10.1016/j.neuron.2018.02.023